1

Flexible Inorganic Light Emitting Diodes Enabled by New Materials and Designs, With Examples of Their Use in Neuroscience Research

Hao Zhang[1]*, Philipp Gutruf*[2]*, and John A. Rogers*[3]

[1] *Northwestern University, Department of Materials Science and Engineering, 2145 Sheridan Road, Evanston, IL 60208, USA*
[2] *University of Arizona Tucson, Department of Biomedical Engineering, 1230 N Cherry Ave., Tucson, AZ 85719, USA*
[3] *Northwestern University, Simpson Querrey Institute for Nano/Biotechnology, Center for Bio-integrated Electronics, Departments of Materials Science and Engineering, Biomedical Engineering, Chemistry, Mechanical Engineering, Electrical Engineering and Computer Science, Civil and Environmental Engineering, 2145 Sheridan Road, Evanston, IL 60208, USA*

1.1 Introduction

Light emitting diodes (LEDs) represent essential components in nearly all solid-state lighting systems. Although conventional LEDs formed from epitaxial materials grown on rigid, brittle, and planar substrates are the most dominant technology, flexible LEDs continue to be of great interest, originating primarily from concepts in flexible, paper-like displays from the 1990s [1]. Flexible LEDs, as defined by their ability to be bent, twisted, and deformed in other ways, also serve as the basis for advanced optoelectronic technologies, ranging from next-generation displays in large or portable formats to wearable/implantable devices capable of intimate contact with soft, curvilinear bio-interfaces. Organic materials, including polymers and small molecules, are natural choices for flexible LEDs due to their favorable mechanical properties, their ability to provide multicolor light emission in ultrathin, lightweight films, and their low-temperature processability and associated compatibility with plastic substrates [1]. Challenges in performance degradation from photooxidation and other subtle effects and their limited color purity remain as key hurdles for organic light emitting diodes (OLEDs). By contrast, LEDs that exploit inorganic semiconductor materials as emissive layers outperform their organic counterparts in terms of brightness, lifetime, efficiency, and color purity. Recent progress in materials designs, fabrication concepts, and assembly approaches now enable high-performance, flexible classes of inorganic light emitting diodes (ILEDs). Integrating these ultrathin components with flexible electronics establishes the basis for system-level, advanced systems for deformable, high-brightness displays and for biomedical tools that provide diagnostic/therapeutic capabilities. The two main approaches toward flexible ILEDs use (i) microscale

Inorganic Flexible Optoelectronics: Materials and Applications,
First Edition. Edited by Zhenqiang Ma and Dong Liu.

ILEDs fabricated from high-quality epitaxial materials grown on source wafers, subsequently released and assembled on flexible target substrates using the techniques of transfer printing, and bridged by structurally optimized interconnects (Section 1.2); and (ii) ILEDs formed with emissive layers composed of solution-processed semiconductors and/or low-dimensional nanomaterials. The former approach mainly relies on processing of well-established, high-performance III–V semiconductors with a novel set of techniques, while the latter deploys diverse classes of new materials, including colloidal semiconductor nanocrystals (or quantum dots [QDs], see Section 1.3), metal halide perovskites (Section 1.4), and two-dimensional (2D) materials (Section 1.5).

This chapter summarizes the most recent advances and key remaining challenges associated with flexible ILEDs from both the materials and device perspectives. The focus is on their unique properties as candidates in flexible ILEDs and state-of-the-art devices design and performance. In addition, recent progress in integrating flexible ILEDs into system-level optoelectronic platforms for various applications highlights the current state of the field. The use of miniaturized, flexible ILEDs to optogenetically modulate neural activity (described in Section 1.6) represents one of the most recent cases.

1.2 Flexible Micro-Inorganic LEDs (μ-ILEDs)

A combination of properties such as brightness, efficiency, color purity, and lifetime makes III–V semiconductor-based LEDs the most attractive candidates for solid-state lighting applications compared to almost all other options, including OLEDs [2, 3]. Existing techniques to incorporate commercial ILEDs into systems such as billboard-scale displays involve robotic, pick-and-place assembly of ILEDs diced from a wafer source, followed by device-by-device, (sub)millimeter-scale packaging, and interconnecting of these components with a collection of bulk wires and heat sinks [4]. These conceptually old techniques are ineffective for assembling ultrasmall (<200 μm × 200 μm, microscale), ultrathin (<50 μm) μ-ILEDs into dense, highly pixelated arrays, particularly on flexible substrates. A set of unconventional processes, starting with the rational design of the μ-ILEDs in released configurations but still tethered to the underlying growth wafer, followed by transfer printing to a target substrate, circumvents the abovementioned restrictions [5–9]. This sort of deterministic assembly approach enables the use of μ-ILEDs in a wide range of applications, from high-resolution flexible/deformable displays to cellular-scale biocompatible lighting sources for sensing, therapy, and neuroscience research [4, 10–21]. This section focuses on recent developments in μ-ILEDs, including the materials design and fabrication concepts, as well as their unconventional implementation at circuit and system levels.

The first demonstrations of flexible assembly of μ-ILEDs involved red-emitting AlInGaP epitaxial structures. [4] The active layers include emissive quantum wells (6 nm thick $In_{0.56}Ga_{0.44}P$ wells, with 6 nm thick barriers of $Al_{0.25}Ga_{0.25}In_{0.5}P$ on top and at the bottom), cladding films, spreaders, and contacts, all grown on GaAs source wafers via metal organic chemical vapor deposition techniques with high levels of control over the doping profiles (layer configuration shown in Figure 1.1a). Multiple photolithography and selective etching steps define the lateral dimension (as small as 25 μm × 25 μm) and yield isolated arrays of ILEDs. After selective removal of the underlying sacrificial layer (AlAs) by immersion in hydrofluoric acid (HF), the isolated μ-ILEDs remain tethered to the GaAs source substrate via "breakaway" photoresist anchors [4, 18]. Next, a soft elastomeric stamp with engineered features of relief selectively retrieves a set of μ-ILEDs (or solid "inks") from the source wafer ("donor" substrate) and delivers them to a target "receiver" substrate in a desired pattern and in a parallel manner (Figure 1.1a, bottom panel), fully automated using computer-controlled printing systems. This process, referred to as "transfer printing," exploits nonspecific van der Waals interactions at the interface between the solid inks and the relief features on the surfaces of the soft stamps. Detailed descriptions and demonstrations of transfer printing techniques in heterogeneous assembly of highly dissimilar materials can be found in recent reviews [5, 7]. Transfer printing, together with related strategies (e.g. undercut of sacrificial layers, photoresist anchors to tether inks, and chemical design of adhesives [17, 23, 24] to improve the yield of delivery), enables the deterministic manipulation of a large number of μ-ILEDs, each with dimensions that can extend in the range of a few microns in lateral sizes and tens of nanometers in thickness, at room temperature and onto nearly any substrate of interest. Compared to the conventional pick-and-place methods, the soft stamps used in transfer printing enable assembly of material structures and devices that can be smaller, by orders of magnitude, and far more fragile; the parallel operation affords throughput speeds that are many orders of magnitude higher, depending on the layouts. The ultrathin (~2.5 μm in initial demonstrations, and far thinner in more recent demonstrations) form factors of μ-ILEDs allow for the use of standard, planar processing methods to define the conductive interconnects (metals [4, 12, 18] or graphene [25]) in direct or matrix addressable configurations, without the need for wire bonding. Mechanically designed arc-shaped bridges can accommodate strains of ~22% by changing their shapes, thereby allowing for highly stretchable red-emitting μ-ILED displays on polydimethylsiloxane (PDMS) substrates (Figure 1.1b) [4]. Demonstrations of μ-ILED displays of this type show no noticeable changes in color or device performance (e.g. current–voltage characteristics) after up to 500 stretching cycles to strains of >20% (Figure 1.1c) [4].

Further advanced mechanical designs in the interconnect geometries enable arrays of μ-ILEDs to remain operational even under extreme modes of deformation [8, 26]. Figure 1.1d shows an array of μ-ILEDs bridged by serpentine-shaped interconnects. Sandwiching the metal traces between two photodefined layers of epoxy places them near the neutral mechanical plane (NMP), thereby significantly reducing the strains induced by bending [12]. A second cycle of transfer printing can deliver these interconnected μ-ILEDs to prestrained PDMS substrates through selective bonding at specific locations. Releasing the strain leads to a noncoplanar configuration of the serpentine interconnects via processes of mechanical buckling, to further improve the stretchability. The wide range of choices of mechanical design allows stable and robust device operation

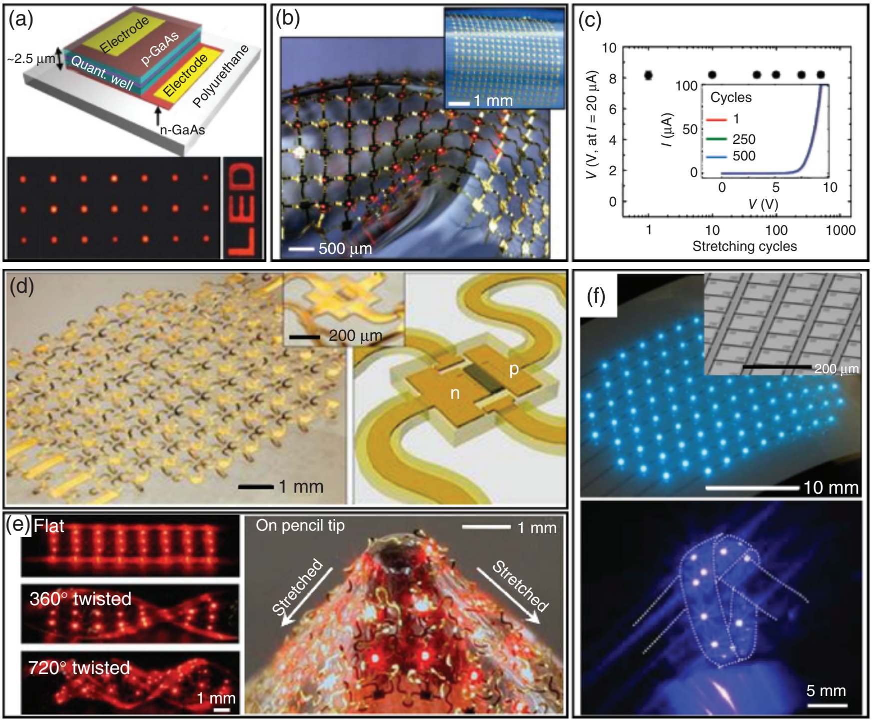

Figure 1.1 *Flexible µ-ILEDs*. (a) (Top) Schematic illustration of an AlGaInP µ-ILED with integrated Ohmic contacts on flexible polyurethane substrate. (Bottom) Optical micrographs of an array of ILEDs (Left: 25 µm × 25 µm, square geometries; Right: characters "LED") in their on state without illumination. (b) Photographs (main and inset) of a passive matrix, stretchable ILED display that uses a noncoplanar mesh configuration, on a rubber substrate. (c) Voltage (V) needed to generate a current of 20 µA measured after stretching cycles to 500 times at an applied strain of 22%. The inset shows the *I*–*V* behavior after these cycling tests. Source: Reproduced with permission from Park et al. [4]. Copyright 2009, The American Association for Advancement of Science. (d) Optical image of a 6 × 6 array of µ-ILEDs (100 µm × 100 µm, and 2.5 µm thick, in an interconnected array with a pitch of ~830 µm) with noncoplanar serpentine bridges on a thin (~400 µm) PDMS substrate (Left-hand frame). Schematic illustration (Right) and corresponding photograph (Inset) of a representative device, with encapsulation. (e) (Left) Optical images of an array of µ-ILEDs (3 × 8) with serpentine interconnects on a band of PDMS twisted to different angles (0° (flat), 360° and 720°). (Right) Optical image of an array of µ-ILEDs (6 × 6), tightly stretched on the sharp tip of a pencil, collected with external illumination. The white arrows indicate the direction of stretching. Source: Reproduced with permission from Kim et al. [12]. Copyright 2010, Nature Publishing Group. (f) (Top) Optical image of a fully interconnected array of InGaN µ-ILEDs on PET. Inset shows the scanning electron microscopy (SEM) image of a dense array of InGaN µ-ILEDs after anisotropic etching of the near-interfacial region of a Si (111) wafer. Source: Reproduced with permission from Kim et al. [15]. Copyright 2011, The National Academy of Sciences. (Bottom) Arrays of GaN µ-ILEDs (12 devices) on a 4 mm × 15 mm strip of PET, tied into a knot to illustrate its deformability. Source: Reproduced with permission from Kim et al. [17]. Copyright 2012, John Wiley & Sons. (g) Illustrations showing the fabrication steps of an array of red-emitting AlGaInP flexible vertical light emitting diodes (f-VLEDs) with multi-quantum well layers. (h) Photographs of a 3 × 3 array of f-VLEDs in a bent state on a glass rod (radius of curvature = 5 mm) and in a flat state (inset). Source: Reproduced with permission from Jeong et al. [22]. Copyright 2014, The Royal Society of Chemistry.

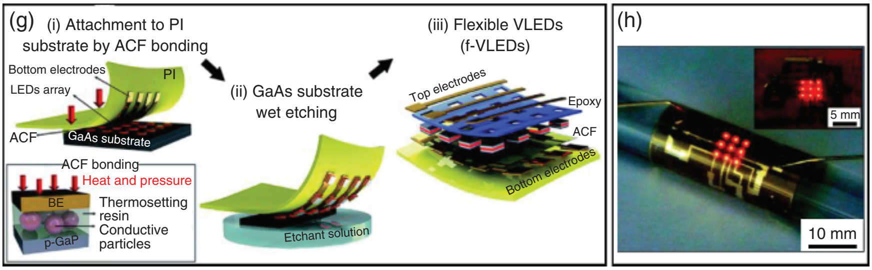

Figure 1.1 (*Continued*)

at repeated, extreme deformational changes (e.g. 100 000 cycles of stretching along the horizontal direction at 75% strain). Besides simple uniaxial stretching, such μ-ILED arrays remain operational under biaxial, shear, twisting, and other mixed distortional modes (Figure 1.1e) [12]. Electrical measurements reveal no measurable changes in current–voltage characteristics after up to 1000 cycles. These optimized mechanical designs enable intimate integration of μ-ILEDs with soft, curvilinear surfaces of human skin/internal organs and on nonplanar surgical tools (e.g. balloon catheters) that involve significant changes in shape during operation, as described later in this section [12, 13].

Similar material designs and fabrication concepts can be extended to blue-emitting μ-ILEDs based on InGaN [15–17]. The high internal quantum efficiency and external quantum efficiency (IQE and EQE greater than 70% and 60%, respectively), long lifetime (>50 000 hours), and luminous efficiency (>200 lm/W) make InGaN LEDs one of the most widespread options in solid-state lighting applications [27]. Depending on the growth substrates, anisotropic wet etching [15] or laser lift-off [16, 17] can be used to separate lithographically defined, isolated μ-ILEDs from their growth wafers. Silicon is of particular interest as a growth substrate due to the availability of large, low-cost wafers and simple schemes for release based on anisotropic etching techniques. Specifically, the large difference (over 100 times) in etching rates of Si(110) compared to Si(111) in a hot potassium hydroxide bath [28, 29] allows for freely suspended, isolated μ-ILEDs where lithographically defined segments of InGaN serve as anchors (Figure 1.1f, inset in top panel) [15]. These approaches bypass the need for conventional laser lift-off techniques, thereby enabling high-throughput, parallel production of millions of devices in forms configured for transfer printing with micron-scale position accuracy. Additionally, the large bandgap of GaN enables a remarkably convenient means for metallization of interconnects, where backside exposure through the transparent active layers yields self-aligned traces without the need for photomasking. The ease in deterministic assembly of ultrathin, ultrasmall (100 μm × 100 μm) blue-emitting μ-ILEDs on target substrates and the straightforward methods for registration of electrical interconnects result in simple routes to large-area, flexible μ-ILED arrays (Figure 1.1f) [15]. Laminating a thin layer of a down-converting phosphor embedded in PDMS and adding a diffuser film on top yield a uniform, white color emission over areas >100 times larger than that of a traditional LED die with the same amount of InGaN.

As an alternate substrate, sapphire is widely used to grow high-quality, state-of-the-art GaN epitaxial layers [17]. Here, separation of patterned μ-ILEDs from the sapphire requires a laser lift-off process. Via a dual transfer printing procedure, μ-ILEDs with dimensions as small as 25 μm × 25 μm can be made with the radiant efficiency up to ~10% in this way. Transfer printing such μ-ILEDs on flexible substrates of polyethylene terephthalate (PET) yields systems with stable operation when strongly bent and twisted (Figure 1.1f, bottom panel) [17]. Moreover, introducing wireless powering components (e.g. a rectangular spiral inductor metal coil) leads to an integrated, implantable blue-emitting μ-ILED array with the ability to operate in a continuous or periodic mode, in a purely wireless manner [16]. This type of system served as the foundation for recent advances in implantable, wireless optogenetic tools for neuroscience, as described in Section 1.6.

In the above cases, the assembly of μ-ILEDs relies on their release from a source wafer via selective etching or laser lift-off, followed by deterministic

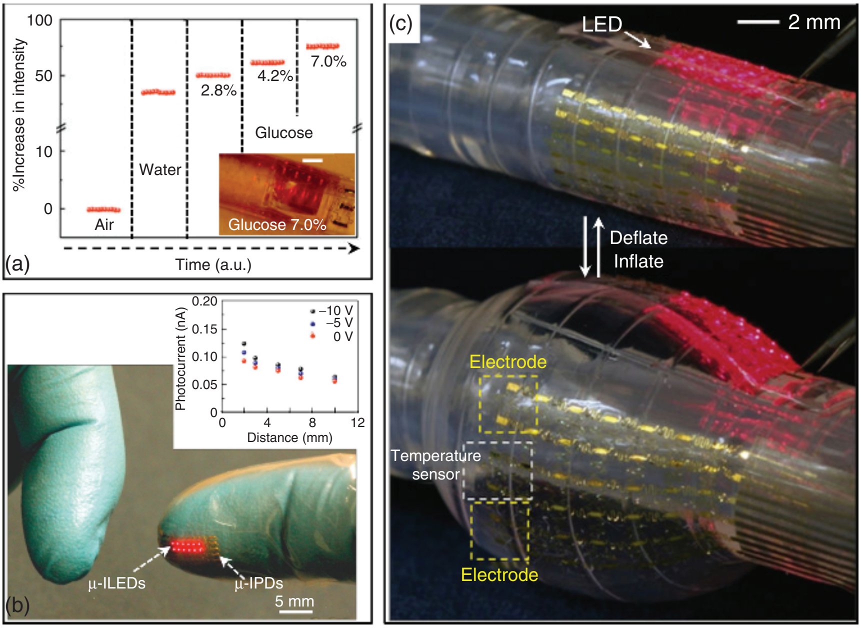

Figure 1.2 *Flexible μ-ILEDs: Examples of integrated devices in biomedical applications*. (a) Measurement results from a representative refractive index microsensor. (Inset) The sensor integrates a μ-ILED array and molded plasmonic crystals and laminates directly on a flexible plastic tube with a sequence of glucose solutions passing through. Scale bar = 1 mm in inset. (b) Optical image of a proximity sensor with arrays of μ-ILEDs (4 × 6) and μ-IPDs, transfer printed on the fingertip region of a vinyl glove. The inset shows a plot of photocurrent as a function of distance between the sensor and an object (white filter paper) for different reverse biases and different voltages. Source: Reproduced with permission from Kim et al. [12]. Copyright 2010, Nature Publishing Group. (c) Optical image of a multifunctional balloon catheter in deflated and inflated states. The image shows arrays of temperature sensors (anterior), μ-ILEDs (posterior), and tactile sensors (facing downward). Source: Reproduced with permission from Kim et al. [13]. Copyright 2011, Nature Publishing Group.

assembly via transfer printing. An alternative approach (Figure 1.1g) [22, 30] requires no sacrificial layers or transfer printing steps. Here, red-emitting AlGaInP epitaxial layers grown on GaAs wafers bond to a thin polyimide layer (PI, 25 μm, preprinted with bottom electrodes) via an anisotropic conductive film (ACF). Subsequent wet etching removes the entire GaAs wafer and exposes the epitaxial structures for further epoxy passivation and top electrode deposition. The resulting red-emitting, flexible vertical μ-ILEDs on PI substrate remain operational in the bent form (bending radius, 5 mm) (Figure 1.1h) [22]. A disadvantage of this approach is that it consumes the growth wafer, thereby preventing its reuse for additional cycles of growth.

A key feature of these types of flexible μ-ILEDs is that they can conformally laminate onto curvilinear surfaces and find use in several unconventional applications, especially those in biomedical sensing, physiological monitoring, and clinical therapy. For example, a stretchable μ-ILED array integrated with molded plasmonic crystals and an external photodetector offers capabilities in the quantitative monitoring of changes in refractive indices of fluids that pass through tubing, which is of relevance for use in intravenous delivery systems for continuous monitoring of nutrient dosage (Figure 1.2a) [12]. In another example, a flexible device with both μ-ILEDs and micro-inorganic photodetectors (μ-IPDs) mounted on the fingertip of a glove serves as an optical proximity senor (Figure 1.2b) [12]. Encapsulation with biocompatible, PDMS layers renders these flexible μ-ILEDs waterproof and operational even when completely immersed in bio-fluids, allowing their use in implantable systems [12]. Flexible μ-ILEDs and a collections of other interconnected devices can be mounted on commercial balloon catheters, for the sensing of a variety of physiological parameters as well as electrically and/or thermally stimulating tissues at the bio-interface (Figure 1.2c) [13].

1.3 Flexible Quantum Dot LEDs (QLEDs)

QDs are semiconductor nanocrystals with sizes in the quantum-confined regime (usually in the range of 2–20 nm) [31, 32]. The discrete, quantized energy levels lead to well-known size-dependent optical properties (Figure 1.3a) [33]. The most enabling features of QDs as LED emitters are their broad spectral tunability (from UV to near infrared [NIR]) and narrow emission peaks (full width at half maximum [FWHM] smaller than 30 nm). Additionally, as with organic materials, QDs in colloidal form can be well dispersed in solvents and are amenable to a series of low-cost, solution-based techniques to assemble into large-scale solid-state materials [34, 41]. These attributes, especially their exceptional color purity and extended color gamut, motivate research into electroluminescent (EL) quantum dot-based light emitting diodes (QLEDs) as alternatives to OLEDs, with initial work published more than two decades ago [42, 43]. On the other hand, applications that harness optically induced emission (or photoluminescence [PL]) of QDs in backlighting for liquid crystal displays or as downconverters in solid-state lighting sources have evolved into mass-produced consumer products, including the Samsung Quantum Dot TV and Amazon Kindle Fire HDX 7 Tablet [44].

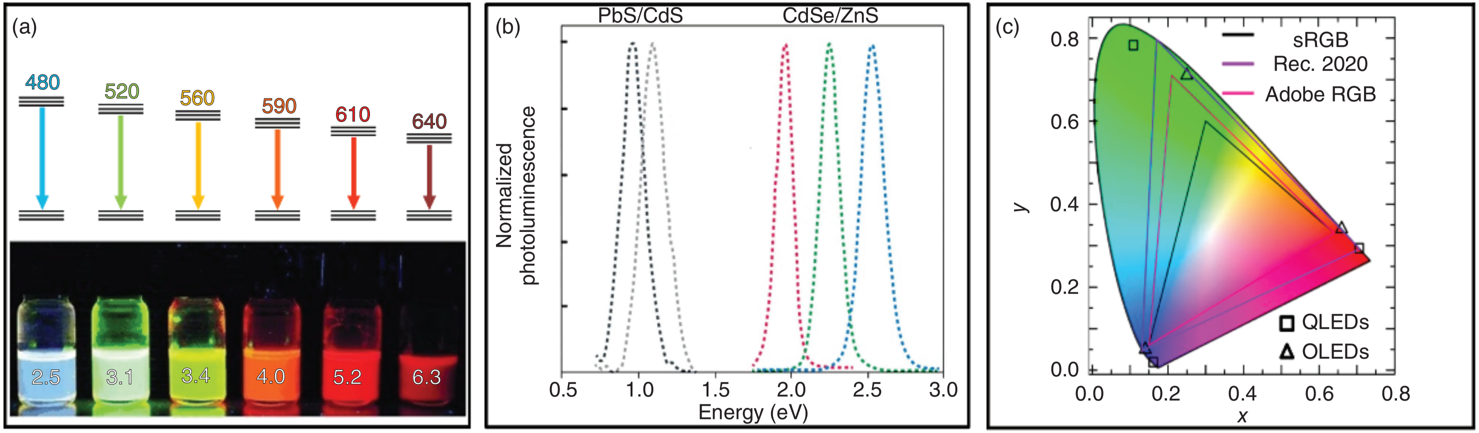

Figure 1.3 *Flexible QLEDs: Materials designs, fabrication techniques, and bendable QLEDs*. (a) (Top) Schematic diagram of bandgap and (bottom) emission color as a function of size of CdSe QDs. Source: Reproduced with permission from Goesmann and Feldmann [33]. Copyright 2010, John Wiley & Sons. (b) Photoluminescence (PL) spectra of CdSe/ZnS and PbS/CdS core/shell colloidal QDs, demonstrating the size- and composition-dependent tunability of QD emission color. Source: Reproduced with permission from Shirasaki et al. [34]. Copyright 2013, Nature Publishing Group. (c) Representative RGB color spaces (solid lines) and chromaticity points of RGB QLEDs (squares) and cutting-edge OLED products (triangles) relative to the CIE 1931 chromaticity diagram. While the state-of-the-art OLEDs can only cover sRGB or Adobe RGB color space with the help of optical engineering, QLEDs easily meet the current standards and satisfy Rec. 2020. Source: Reproduced with permission from Pietryga et al. [35]. Copyright 2016, American Chemical Society. (d) Band engineering of QDs by forming heterostructures. Representative transmission electron microscopy (TEM) images and band structures of (Left) core/shell (continuously graded CdSe/$Cd_xZn_{1-x}Se/ZnSe_{0.5}S_{0.5}$) QDs. Scale bar in the TEM image: 10 nm. Source: Reproduced with permission from Lim et al. [36]. Copyright 2018, Nature Publishing Group. (Right) Representative TEM image and band structures of DHNRs. Scale bars in the TEM image and the inset: 50 and 5 nm. Source: Reproduced with permission from Oh et al. [37]. Copyright 2014, Nature Publishing Group. (e) Intaglio transfer printing for high-resolution RGB QLEDs. (Left) The PL image showing aligned RGB pixels (2460 ppi with the pixel size of 6 μm). (Right) The PL image of the RGB QD patterns via multiple aligned transfer printings. Source: https://creativecommons.org/licenses/by/4.0/, [38]. (f) Composite fluorescence images of electrohydrodynamic jet (E-jet) printed dual-color QD patterns. Inset shows an optical microscope image of a metal-coated glass nozzle (5 μm inner diameter at the tip) and a target substrate during the E-jet printing. Source: Reproduced with permission from Kim et al. [39]. Copyright 2015, American Chemical Society. (g) A typical device structure and energy band diagram of flexible QLED using inorganic/organic hybrid charge transporting layers. (h) Flexible full color QLED with RGB pixels (inset) patterned by transfer printing onto polyethylene naphthalate substrate. Inset: optical image of simultaneous electroluminescence emission of RGB patterned QDs. Source: Reproduced with permission from Kim et al. [40]. Copyright 2011, Nature Publishing Group. (i) Optical image of the flexible white QLEDs made by Intaglio transfer printing under the bias. Bending radius is 1 cm. Source: https://creativecommons.org/licenses/by/4.0/, [38].

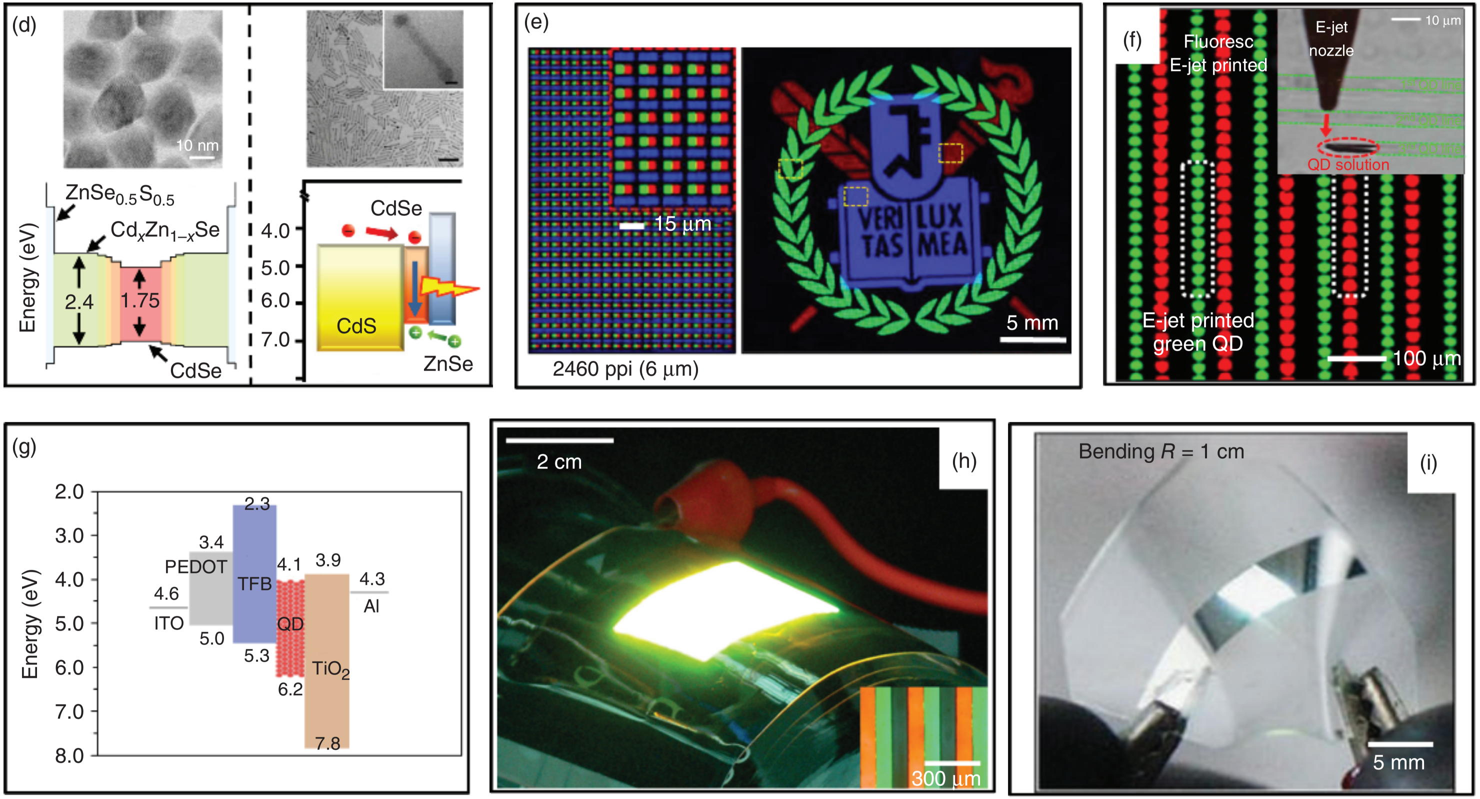

Figure 1.3 (*Continued*)

Progress in QLEDs can be found in several recent reviews [34, 35, 45, 46]. This section begins with a brief introduction to the unique optical properties of QDs and focuses on the most recent advances of flexible QLEDs and their applications in high-resolution displays as well as wearable, skin-mounted devices.

A wealth of well-established synthetic protocols (primarily wet chemistries) can yield QDs with tunable emission properties spanning the entire visible spectrum and NIR. A combination of QD sizes, compositions, heterostructures, as well as surface chemistry offers superior control of QD emission characteristics:

(i) *Spectral tunability*. Cadmium selenide (CdSe) QDs with different sizes (2.5–6.3 nm, smaller than the Bohr radius of bulk CdSe) exhibit different colors as a result of size-dependent bandgaps (Figure 1.3a) [33, 47]. The spectral tunability also comes from changes in compositions/stoichiometries, as exemplified by CdSe- and PbS-based QDs (Figure 1.3b) [34]. Efficient emission in the NIR regime afforded by IV–VI [48, 49], III–V [50, 51], and other QDs provides a distinct advantage over organic-based fluorophores.

(ii) *Color purity*. High-quality, monodisperse QDs (size distribution within 5%) exhibit narrow emission (FWHM < 30 nm compared to 40–60 nm in OLEDs) and thus a wider color gamut, meeting the Rec. 2020 standard for ultrahigh definition TV (Figure 1.3c) [34, 35, 45].

(iii) *Brightness*. As with conventional LEDs, the brightness or the radiant efficiency of QLEDs is closely related to EQE, which depends on the injection of charge carriers, light emission (quantified by quantum yield, defined as the ratio of radiative recombination rate to the sum of rates of radiative and nonradiative recombination), and light out-coupling. Advanced synthetic procedures enable the formation of heterostructures, such as core–shell QDs [36, 52, 53], double heterojunction nanorods (DHNRs) [37, 54, 55], and many others, in a precisely controlled manner at the nanometer scale (Figure 1.3d). Core–shell QDs with near unity quantum efficiency are the most widely used materials in QLEDs [56, 57]. More sophisticated, anisotropic DHNRs feature two larger bandgap semiconductors (CdS and ZnSe) with type II band offset surrounding and in contact with a smaller bandgap (CdSe) emitting center [37]. This material design allows independent control over the electron and hole processes, and more interestingly, increases the upper limit on light out-coupling due to the anisotropic optical properties [54]. Details of the underlying mechanism that correlates heterostructure designs to enhanced EQEs can be found in a recent review [35]. The optimized compositional, structural, and surface control of QDs yields QLEDs with high efficiencies and brightness on par with the state-of-the-art OLEDs (record EQE and brightness for QLEDs: red: 20.2% [58], 106 000 cd/m^2 [59]; green: 14.5% [60], 218 800 cd/m^2 [61]; blue: 10.7% [60], 7600 cd/m^2 [62]).

Fabrication of emissive QD layers in monochromic QLEDs typically exploits spin-casting processes. These same techniques are not, however, amenable to the fabrication of RGB pixelated, full color displays due to cross-contamination/redissolution that can arise during sequential steps in spin-casting. Transfer printing methods, similar to those described for μ-ILEDs, provide effective routes to pixelating QDs [38, 53, 63–65]. Here, an elastomeric stamp (typically PDMS) delivers a uniform QD film (either spin-cast on a stamp

[65] or peeled off from a donor substrate [40, 63]) to a target substrate in a deterministic, parallel manner. In one example, this solvent-free method enables placement of RGB pixels (46 μm × 96 μm) across a 4-in. display with 320 × 240 pixels (corresponding to 100 pixels per inch, or 100 ppi) [40]. The stamps can lead to discrepancies between the designed and printed QD patterns, especially for high-resolution geometries and small pixel sizes (e.g. below 35 μm) [38]. An alternative form of transfer printing process addresses this limitation with the use of an intaglio trench that allows high-resolution (2460 ppi), full color displays with uniform, ultrasmall RGB pixels (as small as 5 μm, Figure 1.3e) [38]. The high fidelity follows from the gentle contact between the QD thin film on the stamp and the intaglio trench, and subsequent slow delamination. During this process, cracks occur at the sharp edges of the trenches and only the noncontacting part of the QD layer (with sharp edges) remains on the stamp. The printing yields approach ∼100%, independent of pixel sizes. In addition to transfer printing of the QD layer, schemes now exist for transfer printing of multilayer assemblies (e.g. QD emitting layer/electron transport layer/cathode layer) from a donor substrate to a receiver substrate pre-coated with hole transport layer and anodes, all enabled by the use of a sacrificial fluoropolymer coating [64]. The most enabling feature of this type of multilayer transfer printing is the ability to independently tailor band alignments between the charge transporting layers and QD layers that emit at different wavelengths. As an example, green QDs/TiO_2 and red QDs/ZnO pixels can be sequentially assembled on the same substrate for optimized device performance. Additionally, inkjet printing [39] or 3D printing [66] also provides useful routes to patterning QDs with elaborate designs. For example, inkjet printing enables sequential printing of QDs with different colors in programmable patterns with uniform thicknesses and ultrasmall pixel sizes (5 μm), in a fully automatic manner (Figure 1.3f) [39].

The high performance of QLEDs originates from rational materials design and advanced techniques to assemble ultrathin, high-definition QD emitting pixels. The resulting capabilities serve as the basis for recent advances in flexible QLEDs as next-generation displays as well as their integration with other flexible electronic components for skin-mounted and bio-interfaced applications. An optimized flexible QLED device structure (Figure 1.3g) typically includes a QD emitting layer sandwiched between two hybrid charge transport layers (an inorganic ZnO or TiO_2 electron transport layer and an organic hole transport layer such as poly[(9,9-dioctylfluorenyl-2,7-diyl)-*co*-(4,4′-(*N*-(4-sec-butylphenyl))diphenylamine)], or TFB) [38, 40, 63, 67–69]. This device structure utilizes solution-based deposition of inorganic TiO_2 or ZnO sol–gel nanoparticles at temperatures that are compatible with flexible plastic substrates, in a way that leads to balanced electron/hole injection rates. The first demonstration of flexible QLEDs involved transfer printed RGB pixels on a polyethylene naphthalate (PEN) substrate (Figure 1.3h) [40], with no appreciable changes in luminous efficiency or current–voltage characteristics at a bending radius of 3 cm. Flexible white QLEDs with mixed QD active layers [70] or sequentially stacked RGB layers [63] require sophisticated control of the ratios of QDs of different colors and suffer from low efficiencies due to the inevitable energy transfer between different QDs. Pixelated white QLEDs enabled by intaglio transfer printing circumvent these issues to allow for excellent device performance (true white emission with a maximum EQE of ~1.5%) and stable operation at different bending angles (up to 135°) (Figure 1.3i) [38].

In early examples, flexible QLEDs were typically fabricated on plastic substrates with relatively large thickness (e.g. in the range of hundreds of micrometers for PET [71]), limiting their minimum bending radius to several tens of millimeters [45]. The use of thin tapes of polyimide (Kapton) allows for highly flexible and mechanically robust QLEDs, capable of mounting on and removal from the curved surfaces of many objects [72]. The high efficiency (EQE up to ~4%) and brightness (over 20 000 cd/m^2) largely remain (over 90% of the original brightness) after bending onto a 4 mm diameter rod for 300 cycles. In another example, a double layer composed of parylene and epoxy serves as an ultrathin (~1.1 μm) substrate that is also biocompatible and waterproof [38]. The ultrathin form factor of QLEDs (Figure 1.4a, in total ~2.6 μm) enables various deformations (bending, folding, or crumpling) and conformal integration on human skin as wearable tattoo-like devices. The EQE and brightness (EQE ~ 2.35% at 4.5 V and brightness ~14 000 cd/m^2 at 7 V, Figure 1.4b) are among the highest of reported wearable LEDs and remain stable after 1000 cycles of uniaxial stretching to strains of 20% [38]. Device structure engineering and heterogeneous QD designs further improve the EL performance of flexible QLEDs. Introducing an interfacial layer of polyethylenimine ethoxylated (PEIE) between the green QD emitting layer and hole transport layer in an inverted architecture upshifts the valance band maximum of QDs and favors hole injection, leading to record-high EQE (15.6%) and current efficiency (65.3 cd/A) on glass substrates (Figure 1.4c,d) [71]. Flexible QLEDs on PET using a similar device structure also show a maximum EQE of 8.4% and a current efficiency of 35.1 cd/A, both of which are the highest values reported for flexible QLEDs [71]. On the other hand, green-emitting QDs with relatively thick shells (2 nm thicker compared to conventional core/shell QDs) show drastically suppressed nonradiative Auger recombination, leading to flexible QLEDs with the highest reported brightness (44 719 cd/m^2 at 9 V, Figure 1.4e) [69]. The exceptional electronic and mechanical properties of flexible QLEDs facilitate their integration with other emerging flexible electronic platforms into system-level, skin-mounted devices [68, 69, 73, 74]. One representative example is a smart sensor system capable of monitoring and storing information related to pressure, temperature, and movements, and displaying them in QLED arrays (Figure 1.4f) [69]. Flexible red-emitting QLEDs can also operate as light sources in wearable optical sensors for photoplethysmography (PPG) [73]. A single-step process of transfer printing of the multilayers (Al/TiO$_2$/QD/TFB/graphene/PEN) to a prestrained PDMS substrate, followed by buckling process, results in highly stretchable QLEDs. These devices show no degradation in performance when stretched at 70% strain or folded to a 35 μm bending radius of curvature. Together with an array of PbS QD-based photodetectors, the integrated device can be wrapped around a fingertip to provide in situ monitoring of PPG pulses (Figure 1.4g) [73].

In a broader context, a light-responsive QLED represents an important, recent advance in this field [55]. The ability to combine both efficient photocurrent generation and high electroluminescence within a single system follows from the unique band diagrams in heterogeneous DHNRs (Figure 1.5a). DHNRs contain

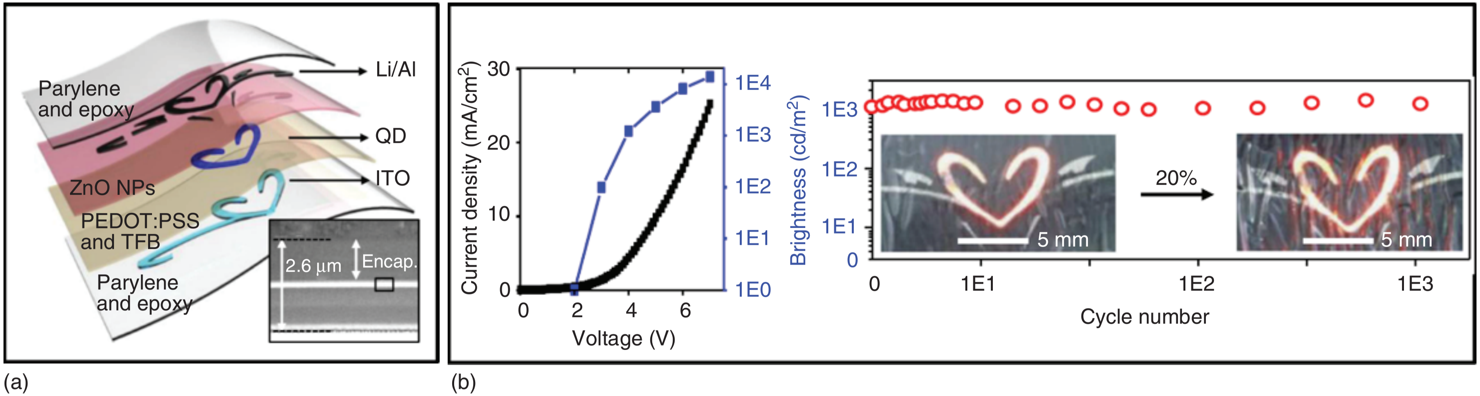

Figure 1.4 *Flexible QLEDs: State-of-the-art devices and their applications in integrated, wearable systems*. (a) Exploded view of the ultrathin, tattoo-like wearable QLED. Inset shows a cross-sectional SEM image in which the thicknesses of the encapsulation and active layers are shown. (b) (Left) The current density–voltage–luminance (*J*–*V*–*L*) characteristics of the ultrathin, wearable QLEDs shown in (a). (Right) Stable brightness in multiple stretching experiments (20%, 1000 times). The inset shows photographs of buckled and stretched ultrathin red QLEDs. Source: https://creativecommons.org/licenses/by/4.0/, [38]. (c) Cross-sectional TEM and stacking sequence of a highly efficient, inverted QLED device with a polyethylenimine ethoxylated (PEIE) interlayer. Top right shows an operating QLED in highly bent state. (d) Current efficiency–EQE–luminance characteristics of inverted QLEDs without and with 15.5 nm thick PEIE interlayer. Source: Reproduced with permission from Yang et al. [72]. Copyright 2014, American Chemical Society. (e) (Left) Photographs of an ultrathin QLED display based on CdSe/ZnS core/shell QDs with thick shell, in rolled condition and mounted on skin. (Right) *J*–*V*–*L* characteristics of the device. (f) Photographs of (Left) the touch sensor integrated with the ultrathin QLED display and (Right) the integrated wearable system subjected to external heat. Source: Reproduced with permission from Kim et al. [69]. Copyright 2017, John Wiley & Sons. (g) (Left) Skin-mounted photoplethysmographic (PPG) sensor composed of QLEDs during LED operation at 8.4 V and QD photodetectors wrapped around the finger of a subject. (Right) Real-time PPG signal pulse wave measured by a stretchable QD photodetector using the stretchable QLED or an indium tin oxide (ITO)-based rigid QLED as a light source. Source: Reproduced with permission from Kim et al. [73]. Copyright 2017, American Chemical Society.

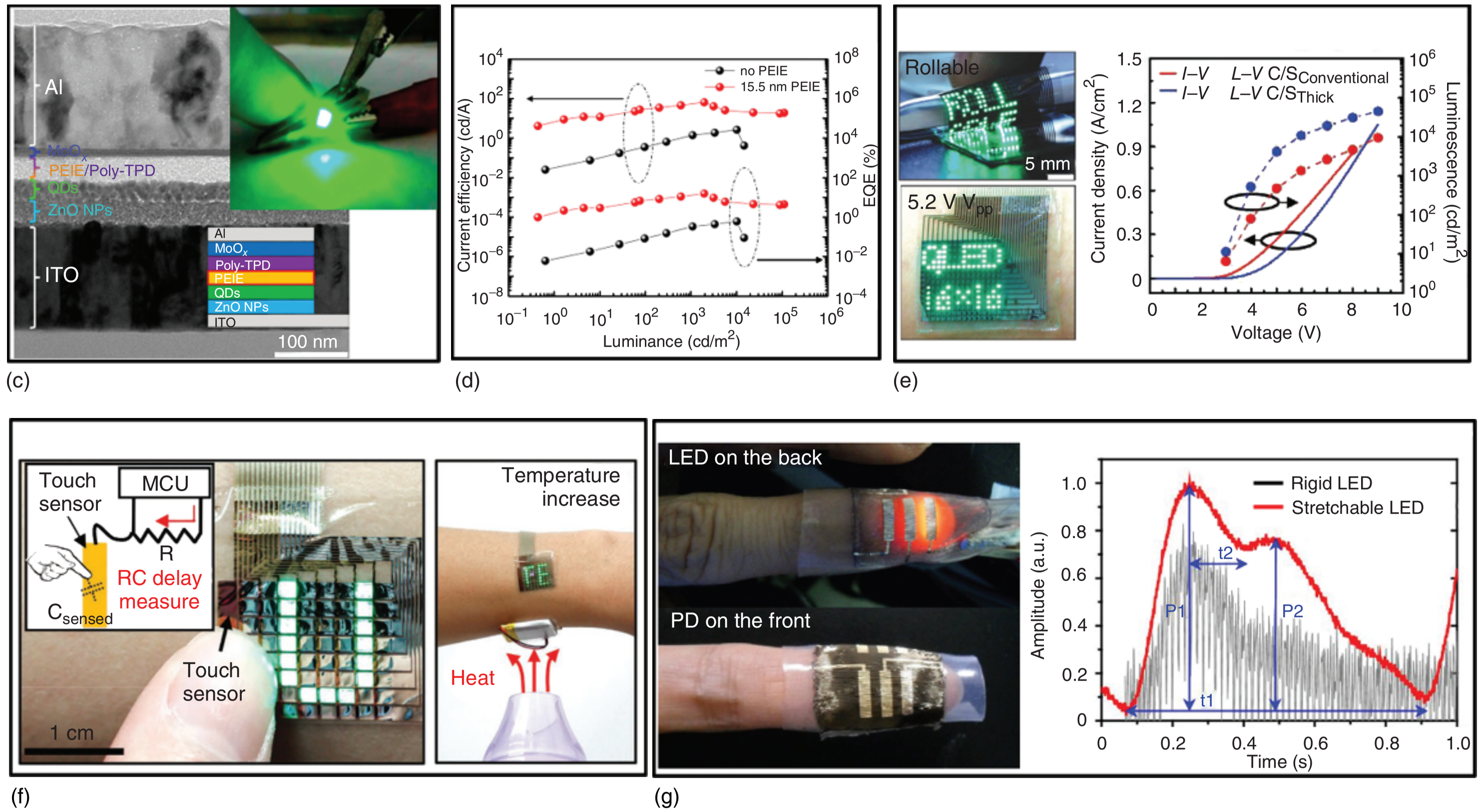

Figure 1.4 (*Continued*)

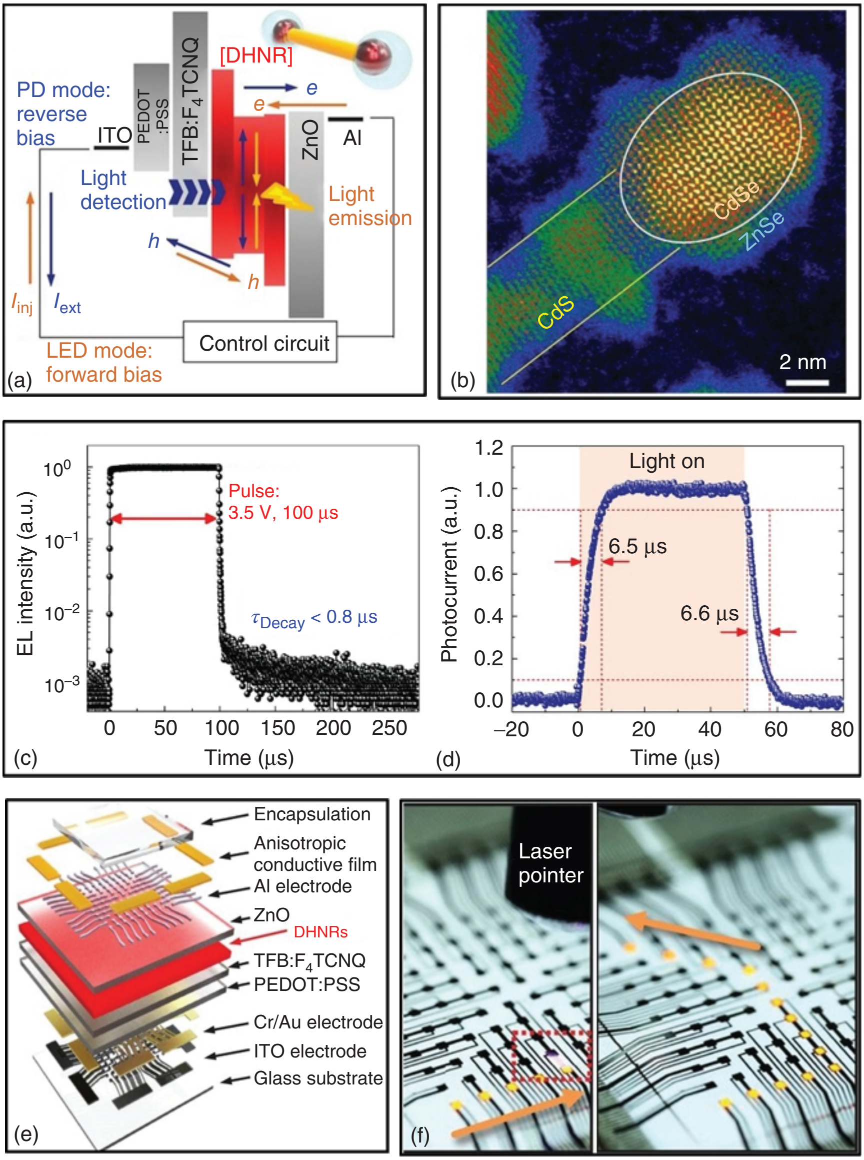

Figure 1.5 *Light responsive, dual-functional DHNR LEDs*. (a) Energy band diagram of DHNR-LED along with directions of charge flow for light emissive (orange) and detection (blue) and a schematic of a DHNR. (b) A high magnification scanning transmission electron microscopy (STEM) images of DHNRs. (c,d) Transient EL showing decay time and photocurrent in response to illumination by a blue LED source driven by 3 V, 50 μs square-wave voltage pulses. (e) Schematic of a 10 × 10 DHNR-LED array. (f) Photographs of a light-responsive LED array with a laser pointer illuminating and turning on pixels along the path outlined by the orange arrows. (g) Automatic brightness control at the single-pixel level in response to an approaching white LED bulb (Left) or a finger (Right) that blocks ambient light. Source: Reproduced with permission from Oh et al. [55]. Copyright 2017, The American Association of Advancement of Science.

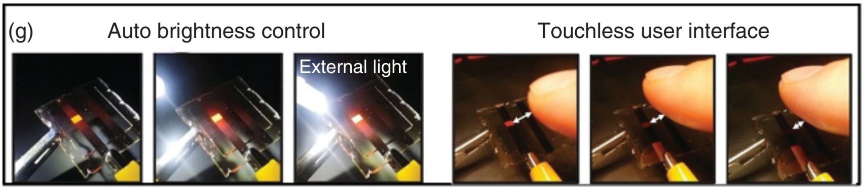

Figure 1.5 (*Continued*)

type-I heterojunctions between the CdSe QDs and two surrounding materials (CdS and ZnSe), which also form type-II offsets by themselves (Figure 1.5b). This band diagram (Figure 1.5a) allows separate control of injection of electron and holes and the more advanced, switchablility between light-emitting and light-detection modes by forward or reverse bias. Figure 1.5c,d demonstrates the temporal response of the dual-functioning DHNR-LEDs. Both EL characteristics (e.g. EQE of 8.0% at 1000 cd/m^2 under 2.5 V bias) and photoresponsivity (e.g. 200 mA/W) of this dual-functional device compare favorably to state-of-the art QLEDs and commercial silicon photodetectors. A multilayered, 10 × 10 pixel device (Figure 1.5e) programmed by a circuit board demonstrates the "writing" action in response to laser excitation (Figure 1.5f). The switchability of the dual modes and the fast response enable their use in touchless displays with automatic brightness control (Figure 1.5g) as well as direct display-to-display data communication systems. Although the reported DHNR-LEDs are fabricated on a glass substrate, the same material/device designs can be extended to flexible light-responsive LEDs.

1.4 Flexible Perovskite LEDs (PeLEDs)

Metal halide perovskites (ABX$_3$, where A is an alkali metal or organic cation, B is typically Pb or other group IV cations, X are halide anions or their mixtures) have attracted tremendous attention in the last several years, primarily due to their rapidly increasing photovoltaic (PV) power conversion efficiencies, from <5% to certified values of 23.3% [75]. The exceptionally high PV performance also promises good light emitting properties according to the Shockley–Queisser detailed balance limit calculations [76, 77]. Perovskite semiconductors feature easily tunable, direct bandgaps via compositional control of anions or cations. The emission spans over a broad spectral range (Figure 1.6a, 390–820 nm) [78]. Unlike QDs, the high color purity of perovskites (FWHM as small as 20 nm) stems from their intrinsic structural similarity to multi quantum wells (MQWs), irrespective of particle/grain size [84, 85]. Additionally, the highly ionic nature of metal halide bonds allows for easy access to a broad range of perovskites from nanoscale materials (sub-10 nm 0D QDs [86, 87], 1D nanowires [88], and 2D nanoplatelets [89]), to polycrystalline thin films with variable grain sizes (sub-100 nm to millimeters) [90, 91], and millimeter-scale, low defect density single crystals [92]. Most of these structures can be synthesized by simple, low-temperature solution-based methods, and in some cases, even in open

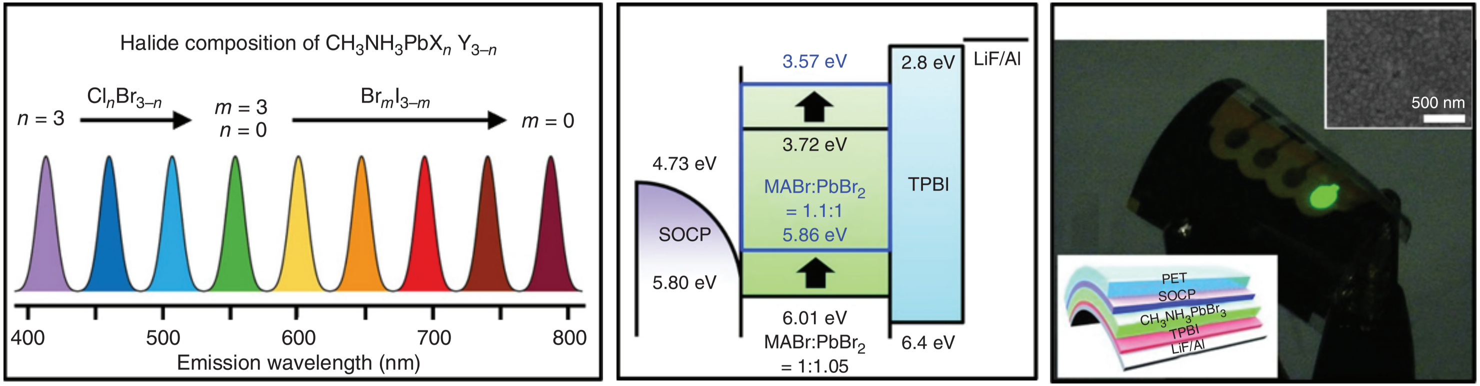

(a) (b) (c)

Figure 1.6 *Flexible PeLEDs*. (a) Emission-wavelength tunability of $CH_3NH_3PbX_nY_{3-n}$. The emission of the $MAPbX_nY_{3-n}$ perovskite is tunable from 390 to 790 nm wavelength. Source: Reproduced with permission from Sutherland and Sargent [78]. Copyright 2016, Nature Publishing Group. (b) Energy band diagram of PeLEDs with $MAPbBr_3$ as the emitting layer, showing a decrease in ionization energy with increasing MABr molar proportion. (c) Photograph of a flexible PeLED on PET substrate with device structure described in (b). (Inset) An SEM image of the $MAPbBr_3$ layer with an average grain size of about 100 nm. Source: Reproduced with permission from Cho et al. [79]. Copyright 2015, The American Association of Advancement of Science. (d) Current efficiency–voltage characteristics of PeLEDs with graphene or indium tin oxide (ITO) as the anode. The inset shows schematic illustration of device structure and efficient light emission in graphene-PeLEDs. (e,f) Normalized current density of flexible graphene- and ITO-PeLEDs on PET substrate according to (e) bending cycle (strain: 1.34%, bending radius: ~7.5 mm) and (f) bending strain. Source: Reproduced with permission from Seo et al. [80]. Copyright 2017, John Wiley & Sons. (g) A flexible, ultrapure green PeLED using 2D $FAPbBr_3$ nanoplatelets as the emitting layer, achieving Rec. 2020 color coordinates. (Left) TEM image of the 2D $FAPbBr_3$ nanoplatelets. Inset shows a photograph of the colloidal $FAPbBr_3$ dispersion with a PL quantum yield of 88%. (Right) Photographs of a flexible perovskite LED at different bending radii (scale bars: 1 cm). Source: Reproduced with permission from Kumar et al. [81]. Copyright 2017, American Chemical Society. (h) SEM images of thin films made from perovskite QDs or polycrystalline grains after bending. Source: Reproduced with permission from Zhao et al. [82]. Copyright 2017, The Royal Society of Chemistry. (i) Photographs of fully printed PeLEDs on polymer substrates. Source: Reproduced with permission from Bade et al. [83]. Copyright 2016, American Chemical Society.

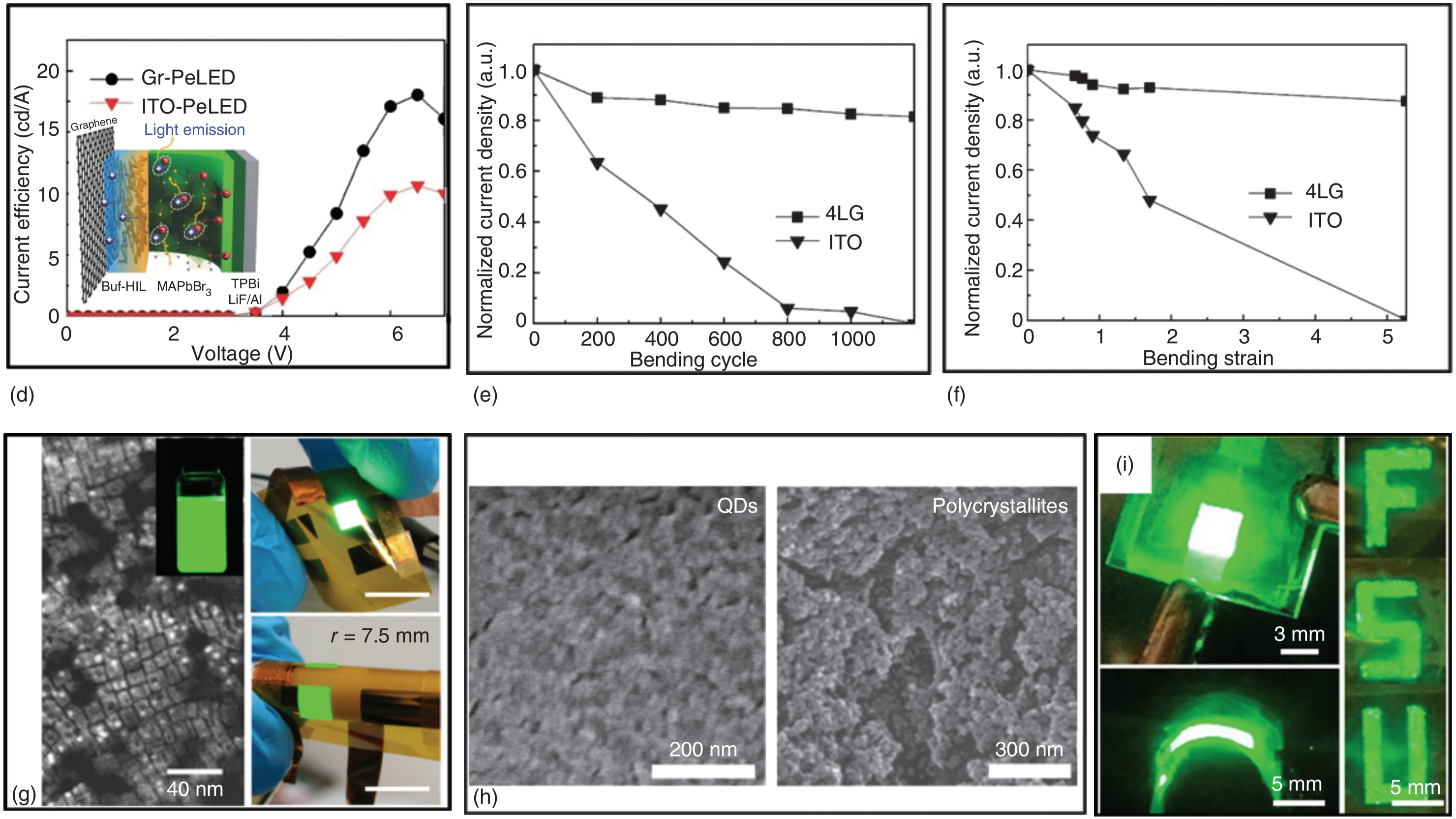

Figure 1.6 (*Continued*)

beakers [86]. The unique optoelectronic properties and simple synthetic and fabrication approaches make perovskites attractive, alternative light emitting materials for LEDs. The long carrier diffusion lengths (∼1 μm) and low exciton binding energies (tens of millielectronvolts) [93] are advantages for the charge carrier separation in high-performance solar cells, but they do not necessarily favor LED performance [79, 84]. Strategies based on grain engineering [79, 80] and chemical design [94–96] can reduce the rates of nonradiative recombination, leading to green and NIR PeLEDs with EQEs exceeding 10% on conventional, rigid substrates [94, 96]. These values are impressive, considering the short history of modern PeLEDs. Research progress related to material designs, fabrication methods, and PeLED performance has appeared in several recent review papers [77, 78, 90]. This section highlights advances in flexible PeLEDs.

Compared to flexible OLEDs or QLEDs, flexible PeLEDs are still in the early stages of development (within five years since the first reports). One of the first demonstrations of flexible PeLEDs exploits methyl ammonium lead bromide ($MAPbBr_3$) as the emissive layer, TPBI (2,2′,2″-(1,3,5-benzinetriyl)-tris(1-phenyl-1-*H*-benzimidazole)) as the electron injection layer, and self-organized conducting polymer (SOCP) as the anode (Figure 1.6b) [79]. Slight excesses of MABr in the synthesis ($MABr:PbBr_2 = 1.1 : 1$) prevents the formation of Pb atom defects and suppresses nonradiative recombination. Adding TPBI molecules, together with the nanocrystal pinning process, hinders the grain growth of $MAPbBr_3$ and confines the excitons in uniform nanograins (average grain size ∼100 nm as shown in the inset of Figure 1.6c, and the carrier diffusion length is ∼67 nm). The grain engineering and compositional control lead to high-performance, green-emitting LEDs with an EQE of 8.53% and current efficiency of 42.9 cd/A. The same strategy and device structure can be extended to a flexible PeLED on PET substrates, as shown in Figure 1.6c. A similar design includes a buffer hole-injection layer (Buf-HIL) and deploys graphene as a flexible anode (Inset in Figure 1.6d) [80]. PeLEDs made on PET substrates with four layers of graphene (4LG) as the anodes exhibit significantly improved mechanical robustness after repeated bending cycles (up to 1200 cycles at 1.34% strain, Figure 1.6e,f).

Another important advance in perovskite materials is the ability to synthesize colloidal perovskite QDs with sizes smaller than 20 nm [86, 87]. Compared to polycrystalline grains, QDs offer an additional degree of freedom in the spectral tunability via quantum confinement. A combination of the intrinsically narrow emission (FWHM 20–25 nm) and precisely controllable bandgap by quantum confinement allows for the “greenest” LED ever reported [81]. In this case, chemically synthesized, 2D $FAPbBr_3$ (FA: formamidinium) quantum wells contain 7–10 unit cells (Figure 1.6g), exhibit a high exciton-binding energy of 162 meV, and emit at an optimal wavelength (∼525 to 530 nm) at a high PL quantum yield (88% and 92% in solution and solid forms, respectively). All of these attributes contribute to an optimized, green-emitting PeLED that covers 97% and 99% of the Rec. 2020 standard in the CIE 1931 and CIE 1976. Ultraflexible devices with bending radii down to 2 mm (bending radius of 7.5 mm shown in Figure 1.6g) also show high-purity green emission. On the other hand, emissive layers composed of sub-10 nm 0D perovskite QDs may provide better mechanical robustness compared to those of polycrystalline perovskites (Figure 1.6h) [82]. A flexible PeLED with a thin film of $MAPbBr_3$ QDs (~7 nm in diameter) as the emissive layer can undergo 1000 bending cycles (bending radius of 4 mm) with an EQE of 2.6% at a brightness of 1000 cd/m^2 [82].

Flexible PeLEDs can also be achieved by screen-printing an emissive layer consisting of $MAPbBr_3$ and poly(ethylene oxide) (PEO) on a polymeric substrate (Figure 1.6i) with carbon nanotubes and silver nanowires as anode and cathode [83]. In the absence of a charge injection/transport layer, the thick (3–4 μm), screen-printed emissive layer ensures very efficient charge carrier injection and transport, as indicated by the low turn-on voltage (2.6 V). Fully printed PeLEDs on 200 μm thick polyacrylate substrates can be bent to radii of ~5 mm, corresponding to 2% applied strain, without notable performance degradation after several cycles.

1.5 Flexible 2D Materials-Based LEDs

2D materials are atomically thin layers with intraplane covalent bonding and interplane van der Waals interactions [6]. Depending on the chemical nature, 2D materials can be conductors (graphene), direct bandgap semiconductors (transition metal dichalcogenides or TMDs, and black phosphorus), and insulators (hexagonal boron nitride, hBN) with optical bandgaps ranging from 0 to 6 eV (Figure 1.7a) [97]. The atomically thin nature of these 2D structures (sub-nanometer scale) makes them promising candidates in flexible optoelectronic devices. For example, the single-layered TMDs exhibit high carrier mobilities (up to ~1000 $cm^2/V\,s$ at room temperature), approaching that of single crystalline silicon, with 2 orders of magnitude thinner profiles and higher strain limits (Figure 1.7b) [6]. The most enabling feature of 2D materials is the freedom to stack multiple atomic layers of dissimilar materials (compositions, band structures, lattice parameters, etc.) through van der Waals interactions for desirable band engineering [102]. These attributes enable application of 2D materials, particularly graphene and TMDs, as the channel semiconductors in flexible, high-performance transistors [97, 103–106], photodetectors [97, 106–108], and as important components (e.g. electrode or charge transport layers) in flexible LEDs [103, 109–112]. This section focuses on recent advances in flexible LEDs with 2D materials as the emissive layers, mainly enabled by materials chemistries and heterostructure designs.

2D emitting materials of particular importance are the TMDs with the chemical formula MCh_2 (M is a transition metal, commonly Mo or W, and Ch is a chalcogen element, S, Se, Te, or mixtures thereof). As single layers, these materials are direct bandgap semiconductors with emission wavelengths in the visible spectrum based on the compositions (Figure 1.7c) [98, 102]. A simple, room temperature chemical treatment (with an organic superacid) uniformly passivates the surface of TMDs, yielding high-quality single layers with nearly unity PL quantum efficiency (Figure 1.7d) [99, 113]. However, this exceptionally high PL efficiency and tunable emission cannot guarantee high-performance LEDs. As a consequence of the lack of Ohmic contacts, EL occurs only around

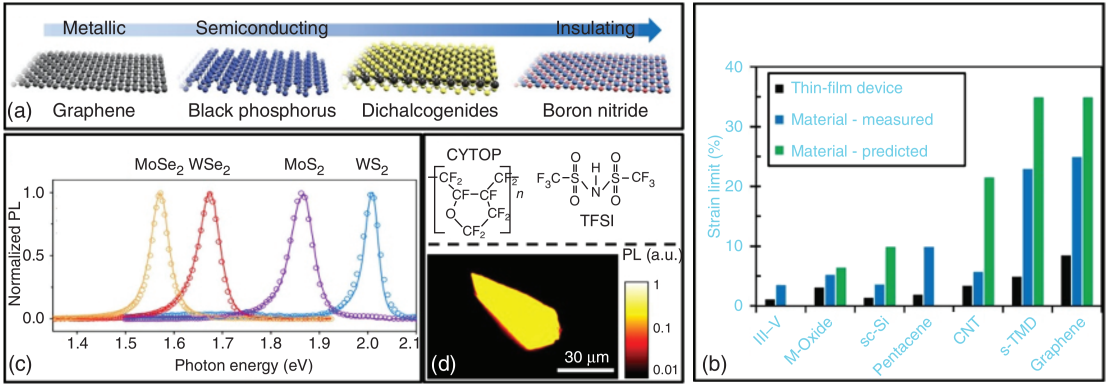

Figure 1.7 *Flexible 2D material based LEDs*. (a) A broad library of 2D layered materials with varying chemical composition, atomic structures, and electronic properties, with an increasing bandgap from left to right. Source: Reproduced with permission from Liu et al. [97]. Copyright 2016, Nature Publishing Group. (b) Comparison of maximum elastic strain limits of 2D materials with other conventional bulk semiconductor materials. Source: Reproduced with permission from Akinwande et al. [6]. Copyright 2014, Nature Publishing Group. (c) EL (lines) and PL (circles) spectra of various transition metal dichalcogenide monolayer devices. Source: https://creativecommons.org/licenses/by/4.0/, [98]. (d) (Top) Molecular structures of CYTOP and TFSI used to encapsulate and treat MoS_2 monolayers for stable, efficient PL. (Bottom) PL image of a MoS_2 monolayer after chemical treatment, showing a near unity PLQY. Source: Reproduced with permission from Kim et al. [99]. Copyright 2017, American Chemical Society. (e) Schematic and STEM image of the multi quantum well (MQW) for heterostructure (hBN/Gr_B/2hBN/MoS_2/2hBN/MoS_2/2hBN/MoS_2/2hBN/MoS_2/2hBN/Gr_T/hBN). The number of hBN layers between MoS_2 QWs in (e) varies. Scale bar, 5 nm. (f) Temperature dependence of EQE for a device with two QWs made from MoS_2 and WSe_2. Inset: Schematic representation of a device with two QWs produced from different materials. (g) Optical images of (top) EL from a single quantum well (SQW) device (hBN/Gr_B/3hBN/MoS_2/3hBN/Gr_T/hBN). $V_b = 2.5$ V, $T = 300$ K and (bottom) a flexible, single quantum well (MoS_2) device on PET taken in reflection mode. Source: Reproduced with permission from Withers et al. [100]. Copyright 2015, Nature Publishing Group. (h) Schematic of the graphene flexible light emitting diode (GFLED). A distinct semi-reduced GO (blue) at the interface between GO (orange) and rGO (gold) is responsible for light emission. (i) Bright red light emission from the all-graphene-based field effect (GFLED) on a flexible PET substrate under a 12 V bias voltage and a 0.1 A drive current. The GFLED size is around 100 µm × 100 µm. The edge of the bent PET is marked by a dashed line. The bending radius is about 8 mm. (j) Schematic of the gate voltage-dependent EL. The Fermi level (orange dashed lines) determines the lowest unoccupied energy state that mainly participates in radiative recombination. Inset: corresponding emission images from a real device. Source: https://creativecommons.org/licenses/by/4.0/, [101].

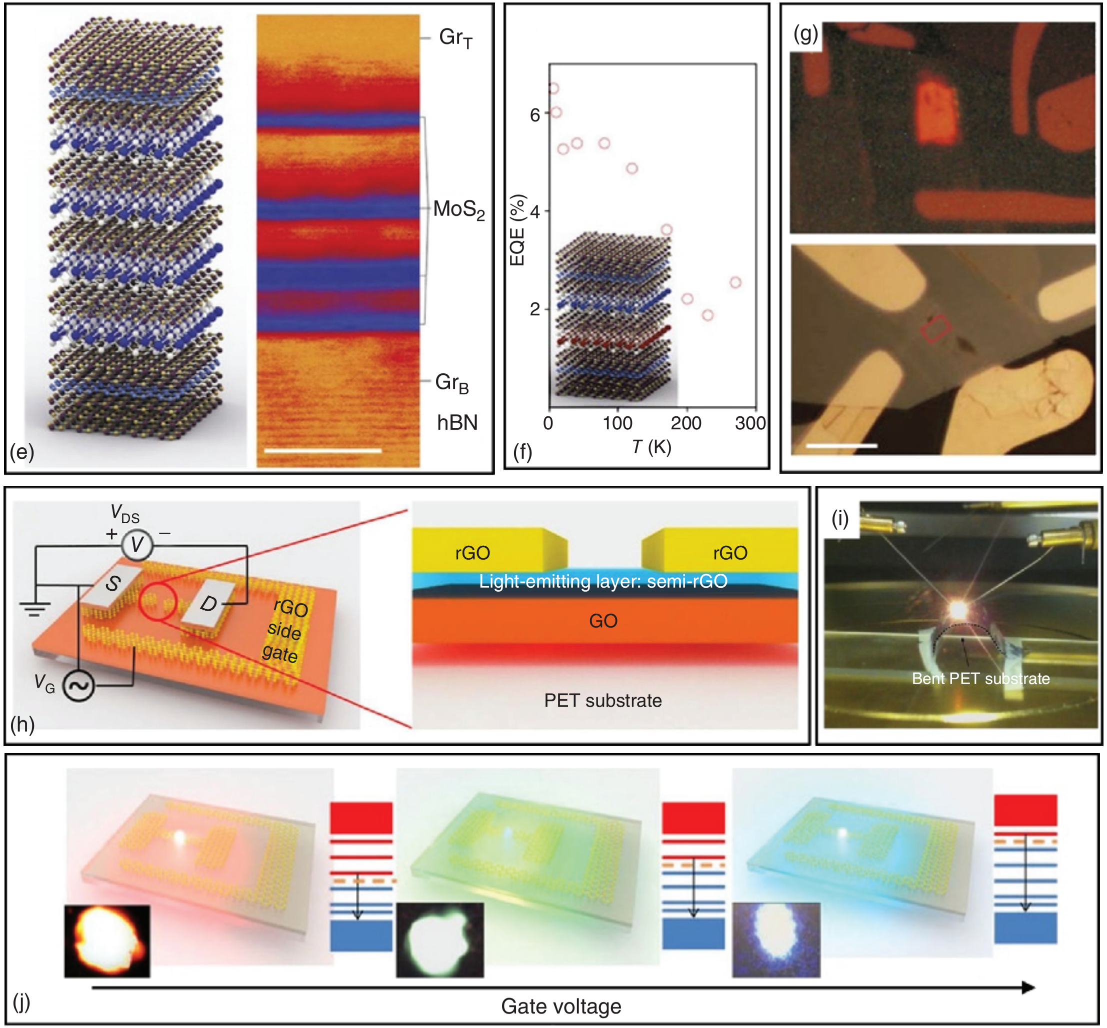

Figure 1.7 (*Continued*)

the contact area due to low carrier injection efficiency [98, 114]. Several strategies have been developed to achieve large-area, steady-state EL, including AC pulse [98], p–n junction formation [115–118], and others. Among these efforts, some of the most significant improvements arise from precisely designed van der Waals heterostructures including vertical stacks of metallic graphene as the electrodes, hBN as the tunneling barriers, and TMDs quantum wells (MoS_2 or WSe_2) as the emissive layers (Figure 1.7e) [100]. The band structure of the heterostructures can be engineered through the selection, numbers, and thickness of each component [100, 119]. Applying a bias to graphene tunes its Fermi level across the TMDs conduction band edge, allowing electrons to efficiently tunnel into the TMDs and radiatively recombine with holes. LEDs with three to four quantum wells show EQEs up to 8.4% [100]. Combining two different TMDs (MoS_2 and WSe_2) allows fine-tuning of the emission spectra with EQEs of about 2% at room temperature (Figure 1.7f), setting record efficiencies for all reported 2D materials-based LEDs. The ultrathin nature (10–40 atoms thick) of the van der Waals structures is well matched to the concepts that underpin flexible electronics. Flexible LEDs fabricated on PET substrates (Figure 1.7g) show unchanged device performance under uniaxial strains up to 1%. Another interesting advancement, though on rigid substrates, exploits vertically stacked n-MoS_2 (1.50 eV)/p-MoS_2 (2.33 eV)/n-GaN (2.58 eV) heterostructures to achieve the first white color emission from 2D materials-based LEDs with a maximum luminance of 30 548 cd/m^2 at 4 V [120].

Graphene-based derivatives also demonstrate EL in transistor configurations (Figure 1.7h) [101]. Versatile carbon chemistries allow for tailoring of the electrical and optical properties of graphene derivatives. Using reduced graphene oxide (rGO) as the gate, source, and drain components, a stack of semi-reduced GO semiconducting layers can produce gate-voltage-dependent EL. Increased gate voltage upshifts the level of the lowest unoccupied energy states and tunes the emission wavelengths from red (750 nm) to blue (450 nm) (Figure 1.7j). Flexible all-graphene-based devices fabricated on PET substrates remain operational at bending radii of ~8 mm (Figure 1.7i). Despite the relatively low brightness (up to 6000 cd/m^2) and efficiency (EQE $<$ 1%), this type of gate-modulated, tunable emission may be attractive for certain applications.

Besides the relatively low device performance, another key challenge for 2D-based (flexible) LEDs follows from the complexity of the growth and fabrication processes. Building van der Waals heterostructures typically relies on mechanical, layer-by-layer stacking of individual layers or through chemical vapor deposition. These methods are not suitable for mass production of structures of arbitrary complexity on flexible substrates. A recent report exploits ink-jet printing technique to form multi-stacked heterostructures using biocompatible, water-based inks for graphene, TMDs, and h-BN. Printed arrays of photodetectors formed in this manner show responsivities higher than 1 mA/W, well above the typical values for devices made with mechanically exfoliated 2D materials [121]. This type of ink-jet printing strategy and the associated ink formulation may also be used to fabricate flexible 2D materials-based LEDs in a high-speed, scalable manner.

1.6 Opportunities for Flexible Optoelectronic Systems in Neuroscience Research

Techniques to genetically target, inhibit, and record from targeted neurons and neural circuits provide essential capabilities in efforts to identify connections between the behavior of animal models and the associated function of neural networks in the brain. The most powerful strategies, known collectively as optogenetics, use light to activate ion channels via opsins expressed in cell membranes by genetic modifications introduced via viral vectors [122]. Together with genetically targeted fluorescent calcium indicators, these methods allow for control and monitoring of specific cell activity in a variety of animal models ranging from small organisms such as worms and fish to large animals such as nonhuman primates [123], across scales ranging from single cells to large neural networks such as the peripherals [124]. Such capabilities lie well outside the scope of non-cell-specific tools such as electrical methods for stimulation and recording [125]. More recent progress, especially in genetically targeted fast voltage sensors [126], has made these optical techniques even more attractive, as they have paved the way for all-optical control of neural systems [127, 128].

With this toolbox of biological techniques, advanced capabilities based on sophisticated photonic and optical schemes for delivering and detecting light in targeted regions of the brain are beginning to emerge, as alternatives to methods that use optical fibers, originally designed for telecommunications [129], delivered into the depths of the brain and affixed with surgical glues, cements, sutures, and external paraphernalia [130–132]. Such technologies will, together with genetically targeted stimulators, inhibitors, and sensors, have significant impact on neuroscience studies by allowing researchers to decipher interactions of the neural system in the brain and peripherals via studies in freely moving animal models [133–135]. Insights from this work and capabilities of these hardware platforms will also drive the development of therapies as unique paths for treating numerous diseases and brain disorders [136]. Progress relies critically on interdisciplinary advances in materials science, optoelectronics, system engineering, and mechanical engineering schemes, as outlined in the previous sections.

Some key system features are displayed schematically in Figure 1.8 [137]. One of the goals is in device miniaturization, to allow full implantation and minimal invasiveness, with complete wireless, battery-free operation to circumvent the limitations of current approaches [137]. The resulting platforms must also be biocompatible in terms of both the chemistry and the mechanics, to allow for stable operation [138] within the demanding set of environments that exist inside biological organisms and its surroundings [139]. Advanced capabilities to deliver multimodal stimulus, ranging from optical to electrical and fluidic, to highly mobile areas of organism such as the peripherals in rodents [140], could serve as the basis of studies including the brain, and extending to other organ systems.

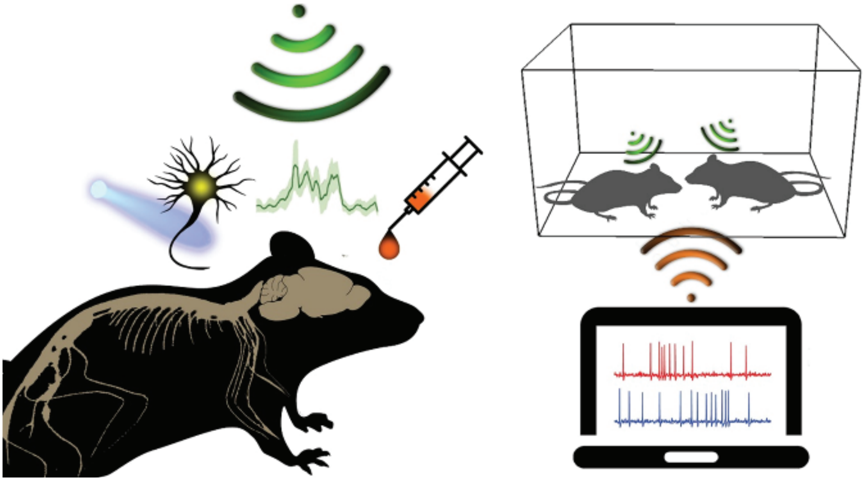

Figure 1.8 Schematic illustration of key stimulus and recording capabilities of wireless multimodal optogenetic tools for neuroscience. Source: Reproduced with permission from Gutruf and Rogers [137]. Copyright 2018, Elsevier.

1.6.1 Miniaturized Flexible LEDs and Detectors for Injectable Neural Probes

The emergence of μ-ILEDs, of the type described in the previous sections, allows delivery of light sources into biological structures directly at the sites of interest, via thin, narrow, flexible filaments introduced in an injection process, as in Figure 1.9a. The extremely small dimensions of the μ-ILEDs, their high efficiency in operation, and natural flow of blood and cerebrospinal fluids allow operation in a manner that does not lead to increases in temperature that might compromise the integrity of the surrounding fragile neural tissues [142, 143]. By comparison to traditional, fiber-based approaches, these platforms offer much smaller dimensions and vastly improved mechanical properties [30], with additional capabilities to receive power from external energy sources for tether-free operation [19].

Illumination profiles associated with such μ-ILED-based probes appear in Figure 1.9b, with direct comparisons to fiber-based systems. Bidirectional as well as unidirectional illumination with μ-ILEDs components and polyimide supports can be realized [19]. Such illumination patterns are advantageous for certain brain geometries in small animal models, such as small oblong-shaped regions in rodents, for example, the basolateral amygdala (BLA) located in the deep brain [141]. For optogenetic stimulation and recording of genetically targeted calcium indicators, illumination profiles, and the resulting localized fluorescence can be predicted using numerical simulations, as shown in the lower bottom panel of Figure 1.9b. Here, absorption and scattering of light with 475 nm wavelength results in activation of opsins such as ChR2 and can also stimulate fluorescence of genetically targeted calcium indicators (GCAMP1-7) within a radius of ~300 μm. Illumination can be controlled by placement, size, and power input, thereby providing drastically improved freedom in design choices over those supported by fiber-based alternatives.

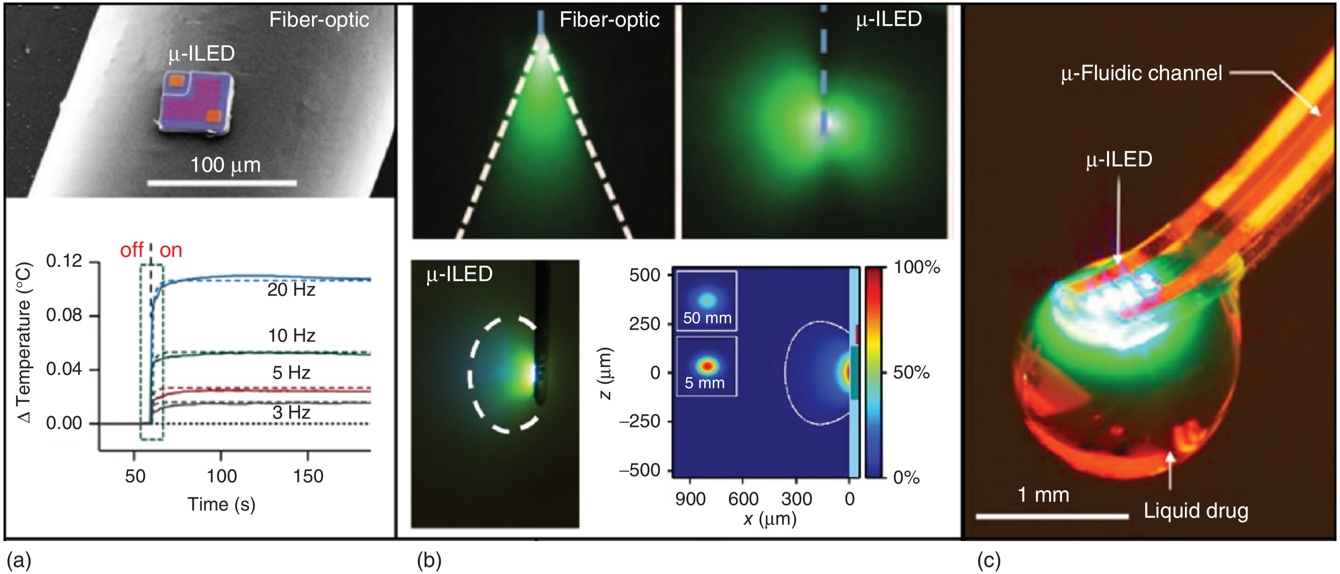

Figure 1.9 *Miniaturized optoelectronic elements for implantable wireless neuroscience tools*. (a) Size comparison and thermal characteristics of a μ-ILED in brain tissue. Source: Reproduced with permission from Kim et al. [19]. Copyright 2013, The American Association of Advancement of Science. (b) Emission characteristics of a μ-ILED mounted on thin filaments benchmarked against fiber-based devices. Source: Reproduced with permission from Lu et al. [141]. Copyright 2018, The National Academy of Sciences. (c) Injectable multimodal platform for optogenetic stimulation and microfluidic drug delivery. Source: Reproduced with permission from Jeong et al. [20]. Copyright 2015, Elsevier. (d) Injectable probe with temperature sensing, optogenetic, photometric, and electrical recording capabilities. Source: Reproduced with permission from Kim et al. [19]. Copyright 2013, The American Association of Advancement of Science. (e) Photometric probe with specific recording capabilities for generically targeted calcium indicators. Source: Reproduced with permission from Lu et al. [141]. Copyright 2018, The National Academy of Sciences.

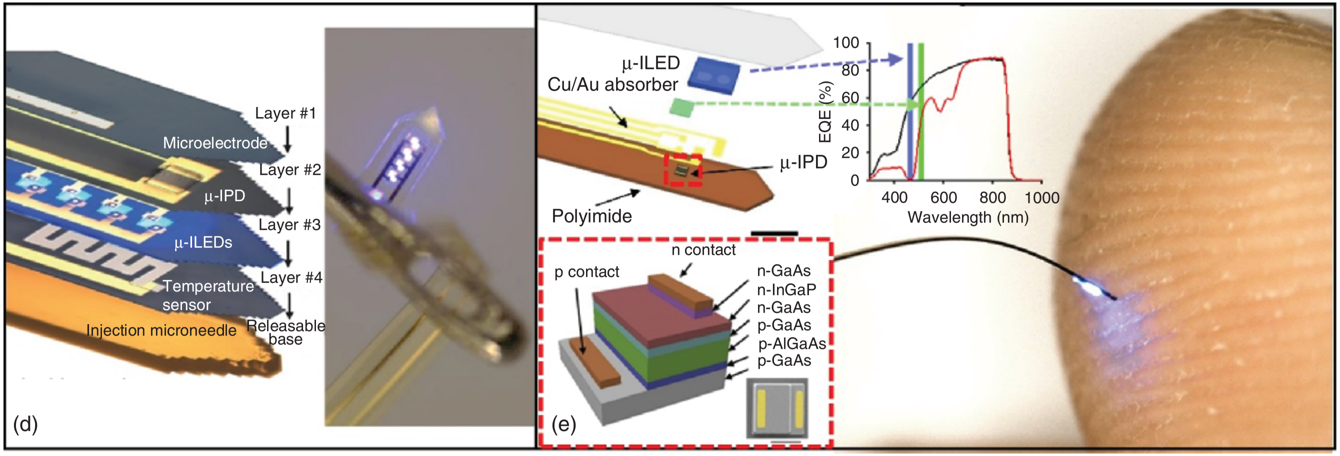

Figure 1.9 (*Continued*)

Heterogeneous fabrication by transfer printing allows the use of plastic filaments to simultaneously support conductive circuitry and optoelectronic elements, with options in multilayer designs for additional functional layers, all in a miniaturized injectable platform. Figure 1.9c shows a demonstration of this type of architecture, where capabilities in optogenetic stimulation unite with those in fluidic delivery. This device allows for the delivery of up to four liquid drugs in separate channels, for spatiotemporal delivery of peptides, viral vectors, and small molecule agents without the severe brain trauma associated with implanted cannulas [20]. The deterministic approach is scalable to more than two layers; an example is shown in Figure 1.9d, where layers with capabilities in temperature sensing, optogenetic stimulation, photometric measurements, and electrical recording appear in a single injectable probe with dimensions smaller than those of conventional unimodal optical fibers [19].

Injectables with advanced optoelectronic components such as photometers allow stimulation and recording of fluctuations in fluorescence associated with genetically targeted calcium indicators, as shown in Figure 1.9e. The results provide indications of the activity of specific cell groups in the deep brain. Here, excitation with a blue μ-ILED stimulates fluorescence captured with an adjacent μ-IPD with an integrated excitation filter aligned to the emission of a genetically targeted sensor (GCaMP6) [141]. The performance of this type of system is comparable to that of conventional fiber-based systems, but with many advantages in tether-free operation, minimal invasiveness, and negligible burden on the animals.

1.6.2 Wireless, Flexible Optoelectronic Systems for Genetically Modified Recording and Stimulation

Miniaturized, high-efficiency light sources can be integrated with compact wireless systems for power and control [144]. Figure 1.10 summarizes some recent efforts to create systems that seamlessly interface with animal models to control and record neuronal populations in the brain. These embodiments represent significant advances over tethered systems in terms of form factor and chronic operation as biocompatible implants.

An example of a fully implantable, battery-free wireless stimulator for spatially and optically separated optogenetic stimulation of the ventral and dorsal regions of the nucleus accumbens shell is shown in Figure 1.10a [145]. The highly miniaturized (5.4 mm × 4.3 mm with thickness of 0.7 mm) soft device features a harvesting antenna with parallel capacitive coupling of adjacent serpentine wires in the overall layout, thereby reducing the antenna area by 100-fold compared to traditional designs. This system allows operation at two transmission frequencies (2.3 and 2.7 GHz) that independently drive blue and green light sources for both optogenetic stimulation and inhibition in a single fully implantable device. Applied to genetically modified animal models, distinct place preference and place aversion patterns, as shown in the bottom panel of Figure 1.10a, can be triggered depending on relative activation of the blue and green μ-ILEDs.

For chronic applications, data show the ability for uninterrupted operation in live animal models for up to one year, as in Figure 1.10b. These highly

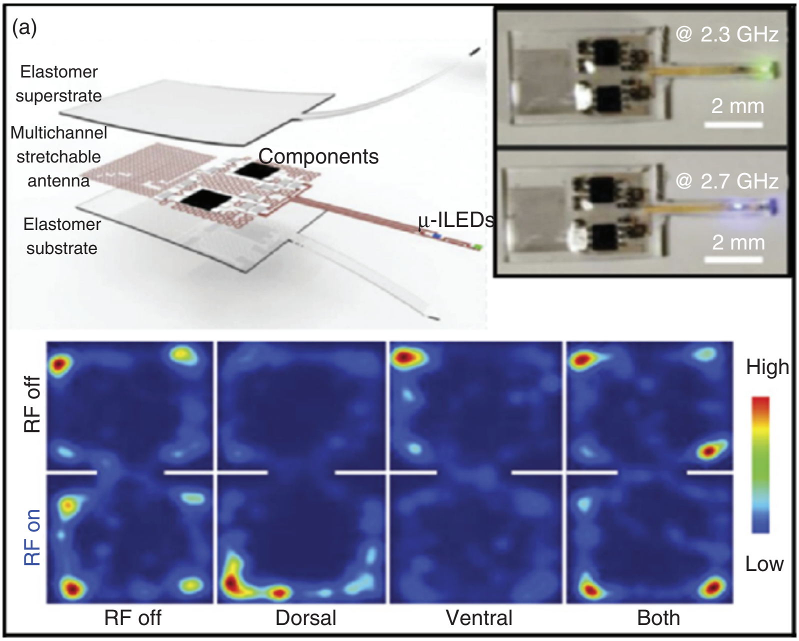

Figure 1.10 *Miniaturized and wireless tools for optogenetic stimulation and recording.* (a) Stretchable and soft subdermally implantable multichannel optogenetic stimulation device. Experimental demonstration of selective stimulation of ventral and dorsal brain regions of the nucleus accumbens shell causing place aversion and preference as shown in heat maps (Bottom panels). Source: Reproduced with permission from Park et al. [145]. Copyright 2016, The National Academy of Sciences. (b) Thin stretchable monolithically defined subdermally implantable optogenetic stimulator with broad application in multiple animal models. Efficacy of the device is demonstrated in stimulated Cre subjects that express ChR2 in the mesolimbic dopaminergic (DA) terminals of the nucleus accumbens that exhibit place preference as shown in heat maps (bottom left). Source: Reproduced with permission from Shin et al. [146]. Copyright 2017, Elsevier. (c) Multimodal wireless system with capabilities in fluid delivery and optogenetic stimulation with demonstrations in Mu-Opioid induced rotational locomotion and place preference. Source: Reproduced with permission from Jeong et al. [20]. Copyright 2015, Elsevier. (d) Wireless system for recording of genetically targeted calcium indicators with demonstration in measurement of elevated activity in the BLA by foot shock experiments. Source: Reproduced with permission from Lu et al. [141]. Copyright 2018, The National Academy of Sciences.

miniaturized (9.8 mm in diameter and maximum thickness of 1.3 mm, with injectable filament of maximum thickness 75 μm) [146] devices rely on resonant magnetic coupling energy transfer schemes that can be applied to standard place preference setups as in Figure 1.10b, bottom left panel. Additional advantages are the easy adaptability to a variety of enclosures used to analyze subject behavior with respect to subject location, mobility, feeding behavior, and other queues [147] including tests of motor coordination wherein the subjects balance on rotating rods [148] or swim through water mazes [149]. Such tests are now also extendable to social experiments with multiple subjects due to the seamless integration of implant and animal subject shown in Figure 1.10b bottom right

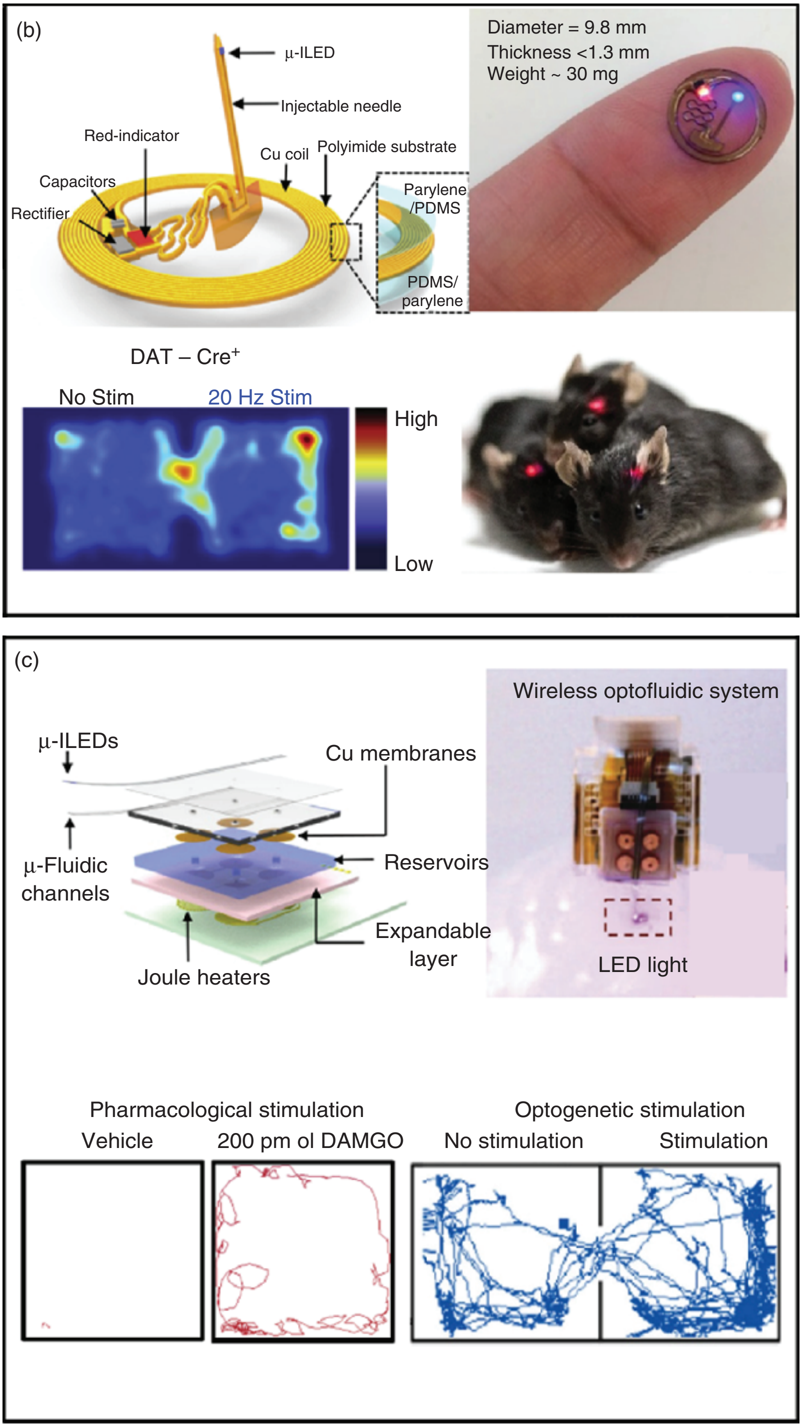

Figure 1.10 (*Continued*)

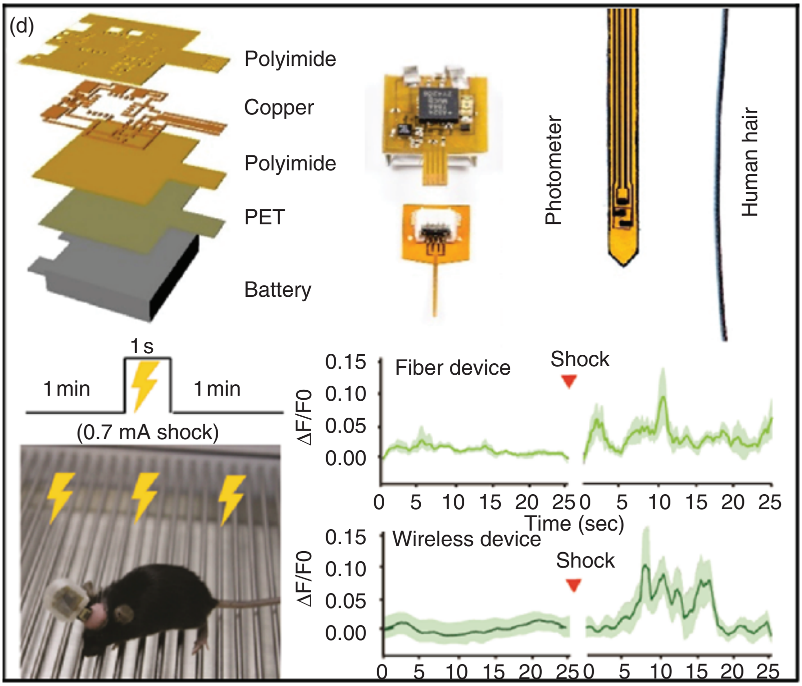

Figure 1.10 (*Continued*)

panel. Conventional fiber or head-mounted systems would result in parasitic, confounding behaviors such as adverse reactions toward subjects with implants.

Systems with multimodal capabilities such as those in microfluidic delivery as described previously can also be realized in wireless miniaturized form factors, such as in the device shown in Figure 1.10c. Pumps that rely on thermal expansion to inject liquid volumes in the microliter range terminate in an injectable that also features μ-ILEDs for optogenetic stimulation [20]. These capabilities create opportunities for experiments that feature the separate, programmed injection of multiple drugs (up to four individually remote controlled). Here, in-subject controls can be used to produce robust experimental outcomes. The bottom panel of Figure 1.10c shows such results where rotational locomotion follows from pharmacological stimuli and place preference from optogenetic stimulus.

An important demonstration for wireless, all-optical control and interrogation of circuit level activity in freely moving subjects is shown in Figure 1.10d. The lightweight (<0.5 g), miniaturized design enables tether-free recording of genetically targeted calcium indicators (GCaMP6) in deep brain regions, namely, the BLA. Such experiments yield insights into the role of this brain region as a hub for processing emotional information with elevated activity in rodents during negative affective states, such as fear and anxiety-like states [141], as shown in the bottom panel of Figure 1.10d. The performance is comparable to that of tethered, fiber-based systems with complex collections of external light sources and control electronics.

1.6.3 Wireless, Battery-Free Optogenetic Stimulation Devices for Use in the Peripheral Nervous System

Potential benefits of optogenetics as a therapeutic tool are especially promising in the peripheral nervous system. Reduction of pain [150], treatment of cardiovascular dysfunction [151], and stimulation of paralyzed muscles [152] are a few recently demonstrated applications. Scalable application in larger animal models and ultimately humans requires suitable means of light delivery. Examples that leverage wireless power transfer in combination with soft systems and μ-ILED technologies can interface with highly mobile areas such as the spine and peripheral nerves, as shown in Figure 1.11.

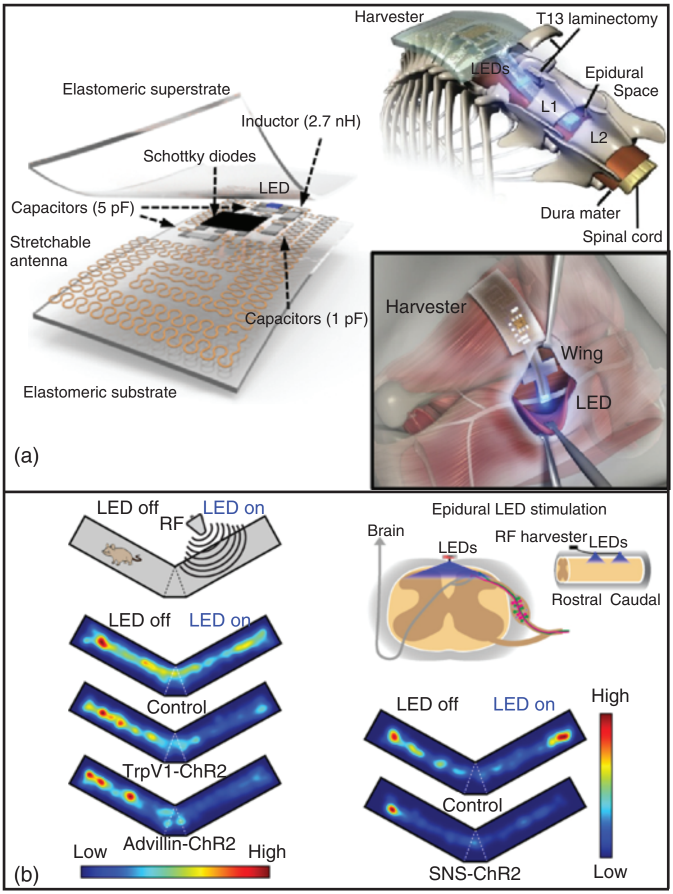

Figure 1.11 *Miniaturized, wireless tools for use in the peripheral nervous System*. (a) Subdermally implantable soft wireless powered optogenetic stimulator for application in the sciatic nerve and epidural space. (b) Resulting heat maps of optostimulation of transgenetic mice exhibiting place preference. Source: Reproduced with permission from Park et al. [144]. Copyright 2015, Nature Publishing Group. (c) Highly miniaturized soft spinal implant and its operational thermal characteristics and effect on animal mobility. Source: Reproduced with permission from Samineni et al. [153]. Copyright 2017, The International Association for the Study of Pain.

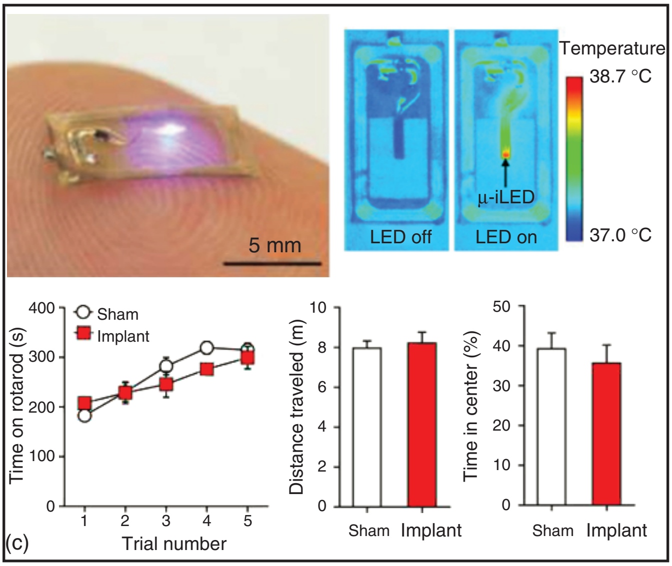

Figure 1.11 (*Continued*)

A lightweight (~16 mg), compact (~16 mm^3), and stretchable (>30% strain) device that can be subdermally implanted and can target the epidural and sciatic nerve in highly active small animal models such as mice with operation of over six months is shown in Figure 1.11a [144]. Successful modulation of pain is demonstrated by a place aversion test shown in Figure 1.11b in animals that express ChR2 in nociceptors with TrpV1 promoter (TrpV1-ChR2) and sensory neuron-specific gene Advillin (Advillin-ChR2) for application in the sciatic nerve and similarly strong response in animals expressing SNS-ChR2 with epidural implants.

Similar results can be achieved with flexible implants that are highly miniaturized but are also constructed using strategies that can support wide distribution to the neuroscience community. With devices of this type, as shown in Figure 1.11c [153], robust optogenetic stimulation can be achieved. Temperature increases associated with the semiconductor components and the antenna structures can be kept to a minimum, as summarized in the thermal image on the right panel of Figure 1.11c, which allows for direct implantation on the spine. This implantation mode allows for animals that are unaffected by the implant, which is shown in the bottom panel of Figure 1.11 where various behavioral assays, such as rotarod and open field test, demonstrate equal activity of animals with and without implants.

1.7 Conclusion

The results highlighted here illustrate the rapid growth in the emerging field of flexible ILEDs, driven by recent advances in materials designs, fabrication concepts, assembly techniques, as well as system-level integration into systems with practical utility. Implementing these high-performance, highly deformable ILEDs into advanced optoelectronic platforms, such as next-generation displays and bio-integrated tools for skin-mounted or injectable applications, presents tremendous opportunities uniquely enabled by these technologies. μ-ILEDs based on rationally designed III–V epitaxial layers and fully automated transfer printing methods represent attractive choices for many of these applications, especially for bio-integrated systems, due to their high brightness and efficiency, which in turn poses minimal thermal load on surrounding tissues, as well as their robustness in operation, their relative insensitivity to air exposure, and their ability for long-term stable operation in biofluids when appropriately encapsulated. These features allow for the realization of injectable filaments for delivery of light to broad classes of biological tissues for selective stimulation of genetically targeted neuron groups. This relocation of the light source to the target site of interest, coupled with technologies to enable localized sensing with highly miniaturized μ-IPDs, facilitates highly miniaturized subdermal implants with capabilities in multimodal dissection of neuronal circuits that enable new paradigms in neuroscience research [146]. On the other hand, flexible ILEDs based on new classes of materials enable low-cost fabrication of flexible, ultrahigh-resolution, full color displays over large areas, and of high color-purity lighting sources. Integrated, wearable smart sensors using QLEDs as displays or light sources represent an appealing type of bio-integrated system for real-time physiological measurements and visualization. Additionally, the unique optical/electronic properties of these emerging materials, following from their favorable underlying physical properties, facile chemical control, and precise structural engineering, open up new possibilities such as dual-functional light-sensitive LEDs [55]. A key challenge for flexible ILEDs based on emerging materials is that most of them rely on toxic elements (e.g. cadmium or lead), which may impede their widespread use especially when incorporated into implantable platforms. Developing heavy-metal-free systems without comprising device performance has been an active topic for QDs and perovskites communities, and success in these endeavors will greatly expedite the use of these flexible ILEDs in bio-integrated systems [35].

Research efforts covered in this chapter establish the foundations for flexible ILEDs encompassing various types of materials as well as their applications at device, circuit, and system levels. The toolbox of design concepts and processing principles developed for ILEDs can also be leveraged in other, related important components (photodetectors, transistors, lasers, etc.), in deformable forms, for advanced optoelectronic platforms. Additional opportunities exist for flexible ILEDs, in both fundamental and applied research, especially those that involve interdisciplinary studies, including synthetic/surface chemistry of materials, novel fabrication/processing techniques, optoelectronic device engineering, mechanical and chemical design at biotic/abiotic interface, biomedical and neurosciences, and others.

References

1 Gustafsson, G., Cao, Y., Treacy, G.M. et al. (1992). *Nature* 357: 477.

2 Gaul, D.A. and Rees, W.S.J. (2000). *Advanced Materials* 12: 935.

3 Nakamura, S. and Fasol, G. (1997). *The Blue Laser Diode: GaN Based Light Emitters and Lasers*. Berlin/Heidelberg: Springer-Verlag.

4 Park, S.-I., Xiong, Y., Kim, R.-H. et al. (2009). *Science* 325: 977.

5 Carlson, A., Bowen, A.M., Huang, Y. et al. (2012). *Advanced Materials* 24: 5284.

6 Akinwande, D., Petrone, N., and Hone, J. (2014). *Nature Communications* 5: 5678.

7 Yoon, J., Lee, S.-M., Kang, D. et al. (2015). *Advanced Optical Materials* 3: 1313.

8 Yoon, J., Baca, A.J., Park, S.-I. et al. (2008). *Nature Materials* 7: 907.

9 He, J., Nuzzo, R.G., and Rogers, J.A. (2015). *Proceedings of the IEEE* 103: 619.

10 Yoon, J., Jo, S., Chun, I.S. et al. (2010). *Nature Materials* 465: 329.

11 Park, S.-I., Le, A.-P., Wu, J. et al. (2010). *Advanced Materials* 22: 3062.

12 Kim, R.-H., Kim, D.-H., Xiao, J. et al. (2010). *Nature Materials* 9: 929.

13 Kim, D.-H., Lu, N., Ghaffari, R. et al. (2011). *Nature Materials* 10: 316.

14 Kim, D.-H., Lu, N., Huang, Y., and Rogers, J.A. (2012). *MRS Bulletin* 37: 226.

15 Kim, H.-S., Brueckner, E., Song, J. et al. (2011). *Proceedings of the National Academy of Sciences of the United States of America* 108: 10072.

16 Kim, R.-H., Tao, H., Kim, T.-I. et al. (2012). *Small* 8: 2812.

17 Kim, T.-I., Jung, Y.H., Song, J. et al. (2012). *Small* 8: 1643.

18 Kim, R.-H., Kim, S., Song, Y.M. et al. (2012). *Small* 8: 3123.

19 Kim, T.-I., McCall, J.G., Jung, Y.H. et al. (2013). *Science* 340: 211.

20 Jeong, J.-W., McCall, J.G., Shin, G. et al. (2015). *Cell* 162: 662.

21 Park, S.I., Shin, G., Banks, A. et al. (2015). *Journal of Neural Engineering* 12: 056002.

22 Jeong, C.K., Park, K.-I., Son, J.H. et al. (2014). *Energy & Environmental Science* 7: 4035.

23 Kim, T.-I., Jung, Y.H., Chung, H.-J. et al. (2012). *Applied Physics Letters* 110: 253104.

24 Kim, T.-I., Kim, M.J., Jung, Y.H. et al. (2014). *Chemistry of Materials* 26: 3502.

25 Kim, R.-H., Bae, M.-H., Kim, D.G. et al. (2011). *Nano Letters* 11: 3881.

26 Kim, D.-H., Ahn, J.-H., Choi, W.M. et al. (2008). *Science* 320: 507.

27 Schubert, E.F. and Kim, J.K. (2005). *Science* 308: 1274.

28 Baca, A.J., Meitl, M., Ko, H.C. et al. (2007). *Advanced Functional Materials* 17: 3051.

29 Bean, K.E. (1978). *IEEE Transactions on Electron Devices* ED-25: 1185.

30 Lee, S.H., Kim, J., Shin, J.H. et al. (2018). *Nano Energy* 44: 447.

31 Kagan, C.R., Lifshitz, E., Sargent, E.H., and Talapin, D.V. (2016). *Science* 353. aac5523.

32 Kagan, C.R. and Murray, C.B. (2015). *Nature Nanotechnology* 10: 1013.

33 Goesmann, H. and Feldmann, C. (2010). *Angewandte Chemie International Edition* 49: 1362.

34 Shirasaki, Y., Supran, G.J., Bawendi, M.G., and Bulovic, V. (2013). *Nature Photonics* 7: 13.

35 Pietryga, J.M., Park, Y.-S., Lim, J. et al. (2016). *Chemical Reviews* 116: 10513.

36 Lim, J., Park, Y.-S., and Klimov, V.I. (2018). *Nature Materials* 17: 42.

37 Oh, N., Nam, S., Zhai, Y. et al. (2014). *Nature Communications* 5: 3642.

38 Choi, M.K., Yang, J., Kang, K. et al. (2015). *Nature Communications* 6: 7149.

39 Kim, B.H., Onses, M.S., Lim, J.B. et al. (2015). *Nano Letters* 15: 969.

40 Kim, T.-H., Cho, K.-S., Lee, E.K. et al. (2011). *Nature Photonics* 5: 176.

41 Talapin, D.V., Lee, J.-S., Kovalenko, M.V., and Shevchenko, E.V. (2010). *Chemical Reviews* 110: 389.

42 Colvin, V.L., Schlamp, M.C., and Alivisatos, A.P. (1994). *Nature* 370: 354.

43 Coe, S., Woo, W.-K., Bawendi, M.G., and Bulovic, V. (2002). *Nature* 420: 800.

44 Boles, M.A., Ling, D., Hyeon, T., and Talapin, D.V. (2014). *Nature Materials* 15: 141.

45 Choi, M.K., Yang, J., Hyeon, T., and Kim, D.-H. (2018). *NPJ Flexible Electronics* 2: 10.

46 Talapin, D.V. and Steckel, J. (2013). *MRS Bulletin* 38: 685.

47 Murray, C.B., Norris, D.J., and Bawendi, M.G. (1993). *Journal of the American Chemical Society* 115: 8706.

48 Talapin, D.V. and Murray, C.B. (2005). *Science* 310: 86.

49 Hines, M.A. and Scholes, G.D. (2003). *Advanced Materials* 15: 1844.

50 Micic, O.I., Curtis, C.J., Jones, K.M. et al. (2005). *Journal of Physical Chemistry B* 109: 18243.

51 Talapin, D.V., Rogach, A.L., Shevchenko, E.V. et al. (2002). *Journal of the American Chemical Society* 124: 5782.

52 Hines, M.A. and Guyot-Sionnest, P. (1996). *Journal of Physical Chemistry* 100: 468.

53 Pal, B.N., Ghosh, Y., Brovelli, S. et al. (2011). *Nano Letters* 12: 331.

54 Nam, S., Oh, N., Zhao, Y., and Shim, M. (2015). *ACS Nano* 9: 878.

55 Oh, N., Kim, B.H., Cho, S.-Y. et al. (2017). *Science* 355: 616.

56 Pu, C. and Peng, X. (2016). *Journal of the American Chemical Society* 138: 8134.

57 Greytak, A.B., Allen, P.M., Liu, W. et al. (2012). *Chemical Science* 3: 2028.

58 Dai, X., Zhang, Z., Jin, Y. et al. (2014). *Nature* 515: 96.

59 Lim, J., Jeong, B., Park, M. et al. (2014). *Advanced Materials* 26: 8034.

60 Yang, Y., Zheng, Y., Cao, W. et al. (2015). *Nature Photonics* 9: 259.

61 Kwak, J., Bae, W.K., Lee, D.C. et al. (2012). *Nano Letters* 12: 2362.

62 Shen, H., Cao, W., Shewmon, N.T. et al. (2015). *Nano Letters* 15: 1211.

63 Kim, T.-H., Chung, D.-Y., Ku, J. et al. (2013). *Nature Communications* 4: 2637.

64 Kim, B.H., Nam, S., Oh, N. et al. (2016). *ACS Nano* 10: 4920.

65 Kim, L., Anikeeva, P., Coe-Sullivan, S.A. et al. (2008). *Nano Letters* 8: 4513.

66 Kong, Y.L., Tamargo, I.A., Kim, H. et al. (2014). *Nano Letters* 14: 7017.

67 Choi, M.K., Yang, J., Kim, D.C. et al. (2018). *Advanced Materials* 30: 1703279.

68 Song, J.-K., Son, D., Kim, J. et al. (2016). *Advanced Functional Materials* 27: 1605286.

69 Kim, J., Shim, H.J., Yang, J. et al. (2017). *Advanced Materials* 29: 1700217.

70 Bae, W.K., Lim, J., Lee, D. et al. (2014). *Advanced Materials* 26: 6387.

71 Kim, D., Fu, Y., Kim, S. et al. (2017). *ACS Nano* 11: 1982.

72 Yang, X., Mutlugun, E., Dang, C. et al. (2014). *ACS Nano* 8: 8224.

73 Kim, T.-H., Lee, C.-S., Kim, S. et al. (2017). *ACS Nano* 11: 5992.

74 Son, D., Chae, S.I., Kim, M. et al. (2016). *Advanced Materials* 28: 9326.

75 Park, N.-G., Gratzel, M., Miyasaka, T. et al. (2016). *Nature Energy* 1: 16152.

76 Miller, O.D., Yablonovitch, E., and Kurtz, S.R. (2012). *IEEE Journal of Photovoltaics* 2: 303.

77 Stranks, S.D. and Snaith, H.J. (2015). *Nature Nanotechnology* 10: 391.

78 Sutherland, B.R. and Sargent, E.H. (2016). *Nature Photonics* 10: 295.

79 Cho, H., Jeong, S.-H., Park, M.-H. et al. (2015). *Science* 350: 1222.

80 Seo, H.-K., Kim, H.-S., Lee, J. et al. (2017). *Advanced Materials* 29: 1605587.

81 Kumar, S., Jagielski, J., Kallikounis, N. et al. (2017). *Nano Letters* 17: 5277.

82 Zhao, F., Chen, D., Chang, S. et al. (2017). *Journal of Materials Chemistry C* 5: 531.

83 Bade, S.G.R., Li, J., Shan, X. et al. (2016). *ACS Nano* 10: 1795.

84 Tan, Z.-K., Moghaddam, R.S., Lai, M.L. et al. (2014). *Nature Nanotechnology* 9: 687.

85 Kim, Y.-H., Cho, H., Heo, J.H. et al. (2014). *Advanced Materials* 27: 1248.

86 Kovalenko, M.V., Protesecu, L., and Bodnarchuk, M.I. (2017). *Science* 358: 745.

87 Protesecu, L., Yakunin, S., Bodnarchuk, M.I. et al. (2015). *Nano Letters* 15: 3692.

88 Zhang, D., Eaton, S.W., Yu, Y. et al. (2015). *Journal of the American Chemical Society* 137: 9230.

89 Bekenstin, Y., Koscher, B.A., Eaton, S.W. et al. (2015). *Journal of the American Chemical Society* 137: 16008.

90 Zhang, W., Eperon, G.E., and Snaith, H.J. (2016). *Nature Energy* 1: 16048.

91 Jeon, N.J., Noh, J.H., Kim, Y.C. et al. (2014). *Nature Materials* 13: 897.

92 Saidaminov, M.I., Abdelhady, A.L., Murali, B. et al. (2015). *Nature Communications* 6: 7586.

93 Stranks, S.D., Eperon, G.E., Grancini, G. et al. (2013). *Science* 342: 341.

94 Yang, X., Zhang, X., Deng, J. et al. (2018). *Nature Communications* 9: 570.

95 Yuan, M., Quan, L.N., Comin, R. et al. (2016). *Nature Nanotechnology* 11: 872.

96 Wang, N., Cheng, L., Ge, R. et al. (2016). *Nature Photonics* 10: 699.

97 Liu, Y., Weiss, N.O., Duan, X. et al. (2016). *Nature Reviews Materials* 1: 16042.

98 Lien, D.-H., Amani, M., Desai, S.B. et al. (2018). *Nature Communications* 9: 1229.

99 Kim, H., Lien, D.-H., Amani, M. et al. (2017). *ACS Nano* 11: 5179.

100 Withers, F., Del Pozo-Zamudio, O., Mishchenko, A. et al. (2015). *Nature Materials* 14: 301.

101 Wang, X., Tian, H., Mohammad, M.A. et al. (2015). *Nature Communications* 6: 7767.

102 Zhang, W., Wang, Q., Chen, Y. et al. (2016). *2D Materials* 3: 022001.

103 Kim, H. and Ahn, J.-H. (2017). *Carbon* 120: 244.

104 Radisavljevic, B., Rdenovic, A., Brivio, J. et al. (2011). *Nature Nanotechnology* 6: 147.

105 Radisavljevic, B. and Kis, A. (2013). *Nature Materials* 12: 815.

106 Gao, L. (2017). *Small* 13: 1603994.

107 Lopez-Sanchez, O., Lembke, D., Kayci, M. et al. (2013). *Nature Nanotechnology* 8: 497.

108 Mak, K.F. and Shan, J. (2016). *Nature Photonics* 10: 216.

109 Choi, M.K., Park, Y.J., Sharma, B.K. et al. (2018). *Science Advances* 4. eaas8721.

110 Choi, G.J., Le, Q.V., Choi, K.S. et al. (2017). *Advanced Materials* 29: 1702598.

111 Shang, J., Cong, C., Wu, L. et al. (2018). *Small Methods* 2: 1800019.

112 Zhou, X., Hu, X., Yu, J. et al. (2018). *Advanced Functional Materials* 28: 1706587.

113 Amani, M., Lien, D.-H., Kiriya, D. et al. (2015). *Science* 350: 1065.

114 Sundaram, R.S., Engel, M., Lombardo, A. et al. (2013). *Nano Letters* 13: 1416.

115 Cheng, R., Li, D., Zhou, H. et al. (2014). *Nano Letters* 14: 5990.

116 Lopez-Sanchez, O., Llado, E.A., Koman, V. et al. (2014). *ACS Nano* 8: 3042.

117 Ross, J.S., Klement, P., Jones, A.M. et al. (2014). *Nature Nanotechnology* 9: 268.

118 Baugher, B.W.H., Churchill, H.O.H., Yang, Y., and Jarillo-Herreo, P. (2014). *Nature Nanotechnology* 9: 262.

119 Palacios-Berraquero, G., Barbone, M., Kara, D.M. et al. (2016). *Nature Communications* 7: 12978.

120 Nikam, R.D., Sonawane, P.A., Sankar, R., and Chen, Y.-T. (2017). *Nano Energy* 32: 454.

121 McManus, D., Vranic, S., Withers, F. et al. (2017). *Nature Nanotechnology* 12: 343.

122 Akerboom, J., Calderón, N.C., Tian, L. et al. (2013). *Frontiers in Molecular Neuroscience* 6: 2.

123 Häusser, M. (2014). *Nature Methods* 11: 1012.

124 Gradinaru, V., Zhang, F., Ramakrishnan, C. et al. (2010). *Cell* 141: 154.

125 Rousche, P.J. and Normann, R.A. (1998). *Journal of Neuroscience Methods* 82: 1.

126 Piatkevich, K.D., Jung, E.E., Straub, C. et al. (2018). *Nature Chemical Biology* 14: 352.

127 Emiliani, V., Cohen, A.E., Deisseroth, K., and Häusser, M. (2015). *Journal of Neuroscience* 35: 13917.

128 Hight, A.E., Kozin, E.D., Darrow, K. et al. (2015). *Hearing Research* 322: 235.

129 Yizhar, O., Fenno, L.E., Davidson, T.J. et al. (2011). *Neuron* 71: 9.

130 Aravanis, A.M., Wang, L.-P., Zhang, F. et al. (2007). *Journal of Neural Engineering* 4: S143.

131 Kravitz, A.V., Freeze, B.S., Parker, P.R. et al. (2010). *Nature* 466: 622.

132 Liu, X., Ramirez, S., Pang, P.T. et al. (2012). *Nature* 484: 381.

133 Seelig, J.D., Chiappe, M.E., Lott, G.K. et al. (2010). *Nature Methods* 7: 535.

134 Voigts, J. and Harnett, M. (2018). *bioRxiv* 262543.

135 Hamel, E.J., Grewe, B.F., Parker, J.G., and Schnitzer, M.J. (2015). *Neuron* 86: 140.

136 Steinbeck, J.A., Choi, S.J., Mrejeru, A. et al. (2015). *Nature Biotechnology* 33: 204.

137 Gutruf, P. and Rogers, J.A. (2018). *Current Opinion in Neurobiology* 50: 42.

138 Jeong, J.-W., Shin, G., Park, S.I. et al. (2015). *Neuron* 86: 175.

139 Hwang, S.-W., Tao, H., Kim, D.-H. et al. (2012). *Science* 337: 1640.

140 Branner, A., Stein, R.B., Fernandez, E. et al. (2004). *IEEE Transactions on Biomedical Engineering* 51: 146.

141 Lu, L., Gutruf, P., Xia, L. et al. (2018). *Proceedings of the National Academy of Sciences of the United States of America* 115: E1374.

142 Li, Y., Shi, X., Song, J. et al. (2013). *Proceedings of the Royal Society of London. Series A* 469: 20130142.

143 McAlinden, N., Massoubre, D., Richardson, E. et al. (2013). *Optics Letters* 38: 992.

144 Park, S.I., Brenner, D.S., Shin, G. et al. (2015). *Nature Biotechnology* 33: 1280.

145 Park, S.I., Shin, G., McCall, J.G. et al. (2016). *Proceedings of the National Academy of Sciences of the United States of America* 113: E8169.

146 Shin, G., Gomez, A.M., Al-Hasani, R. et al. (2017). *Neuron* 93: 509.

147 Cai, H., Haubensak, W., Anthony, T.E., and Anderson, D.J. (2014). *Nature Neuroscience* 17: 1240.

148 Hunt, R.F., Girskis, K.M., Rubenstein, J.L. et al. (2013). *Nature Neuroscience* 16: 692.

149 Merritt, J.R. and Rhodes, J.S. (2015). *Behavioural Brain Research* 280: 62.

150 Draxler, P., Honsek, S.D., Forsthuber, L. et al. (2014). *Journal of Neuroscience* 34: 12015.

151 Vogt, C.C., Bruegmann, T., Malan, D. et al. (2015). *Cardiovascular Research* 106: 338.

152 Bruegmann, T., Van Bremen, T., Vogt, C.C. et al. (2015). *Nature Communications* 6: 7153.

153 Samineni, V.K., Yoon, J., Crawford, K.E. et al. (2017). *Pain* 158: 2108.